

# Lyman- $\alpha$ Visibility During the Epoch of Reionization: Combining JWST FRESCO Grism Data with Keck Archival Spectroscopy

Ecaterina Leonova,<sup>1,2\*</sup> Rohan P. Naidu,<sup>3†</sup> Pascal A. Oesch,<sup>4,5,6</sup> Gabriel Brammer,<sup>5,6</sup> Jorrit Matthee,<sup>7</sup> Romain A. Meyer,<sup>4</sup> Daniel Schaerer,<sup>4</sup> Mengyuan Xiao,<sup>4</sup>

<sup>1</sup>GRAPPA, Anton Pannekoek Institute for Astronomy and Institute of High-Energy Physics

<sup>2</sup>University of Amsterdam, Science Park 904, NL-1098 XH Amsterdam, the Netherlands

<sup>3</sup>MIT Kavli Institute for Astrophysics and Space Research, 70 Vassar Street, Cambridge, MA 02139, USA

<sup>4</sup>Department of Astronomy, University of Geneva, Chemin Pegasi 51, 1290 Versoix, Switzerland

<sup>5</sup>Cosmic Dawn Center (DAWN)

<sup>6</sup>Niels Bohr Institute, University of Copenhagen, Jagtvej 128, DK-2200, Copenhagen N, Denmark

<sup>7</sup>Institute of Science and Technology Austria (ISTA), Am Campus 1, 3400 Klosterneuburg, Austria

Accepted XXX. Received YYY; in original form ZZZ.

## ABSTRACT

The visibility of Lyman- $\alpha$  emission at  $z > 7$  provides crucial insights into the reionization process and the role of galaxies in shaping the ionized intergalactic medium. Using JWST FRESCO data, we investigate the environments of Lyman- $\alpha$  emitters (LAEs) in the GOODS-N and GOODS-S fields by identifying [OIII] emitters and analyzing their large-scale distribution. Using the FRESCO redshifts, we recover eight new LAEs from archival Keck/MOSFIRE observations at  $z = 7.0 - 7.7$ , including a potential AGN candidate at  $z \sim 7.2$ . Complemented by six literature LAEs, our sample consists of 14 LAEs in total, all of which are [OIII] emitters except for one very faint source not detected by FRESCO. We define seven groups of [OIII] emitters centered around the brightest LAEs and find that these bright LAEs do not reside in more overdense environments than the average galaxy population. The overdensity parameters for LAEs and [OIII] emitters without Lyman- $\alpha$ , calculated for sources with  $M_{UV} < -19.5$  to ensure completeness, are similar, indicating that overdensities alone cannot fully explain Lyman- $\alpha$  visibility. While LAEs have slightly higher recent star formation ( $SFR_{10}/SFR_{50} \approx 1.3\times$ ) and [OIII] EW ( $\approx 1.5\times$ ), they show no significant differences from [OIII] emitters in UV slope ( $\beta$ ), UV magnitude ( $M_{UV}$ ), or stellar mass ( $\log_{M_{\star}}$ ). Our results suggest that other factors may contribute to the observability of Lyman- $\alpha$  emission. Future spectroscopic surveys with broader wavelength coverage and more complete sampling will be crucial for refining our understanding of reionization.

**Key words:** galaxies: high-redshift, galaxies: abundances, galaxies: formation, cosmology: reionization, galaxies: groups: general

## 1 INTRODUCTION

Understanding the last major phase transition of the Universe—the Epoch of Reionization (EoR)—is a key goal of extragalactic astronomy. The EoR begins with the first luminous sources that start to ionize their surrounding intergalactic medium (IGM). Early galaxies and stars likely played the driving role in ionizing the hydrogen, leading to the universe’s transition from a predominantly neutral to a fully ionized state by  $z \sim 5.5$  (Barkana & Loeb 2001; Dayal & Ferrara 2018; Robertson 2022).

One of the most effective ways to study the EoR is by observing Lyman- $\alpha$  emitters (LAEs) – galaxies that emit strong Lyman- $\alpha$  radiation at 1215.67 Å (Miralda-Escudé 1998; McQuinn et al. 2007; Dayal

et al. 2011; Mason et al. 2018b; Lu et al. 2024; Napolitano et al. 2024; Prieto-Lyon et al. 2025; Witten et al. 2024; Witsstok et al. 2025). Due to its resonant nature, Lyman- $\alpha$  provides critical information about the neutral hydrogen fraction in the IGM (e.g., Dijkstra 2014; Hutter et al. 2017; Mason et al. 2018a; Hoag et al. 2019; Ouchi et al. 2020; Jones et al. 2025; Kageura et al. 2025). Hydrodynamical simulations also provide important theoretical insight into Lyman- $\alpha$  emission in the early Universe (Smith et al. 2021; Bhagwat et al. 2025; Neyer et al. 2025).

However, detecting LAEs becomes progressively more challenging at higher redshifts, especially beyond  $z > 7$ , when a larger fraction of hydrogen in the universe is still neutral (Stark et al. 2010; Pennericci et al. 2011; Kageura et al. 2025; Tang et al. 2025). Neutral hydrogen scatters Lyman- $\alpha$  photons, which results in suppression of their visibility at high redshifts (e.g., Miralda-Escudé 1998; Dijkstra 2014). The Lyman- $\alpha$  emission from these galaxies is scattered and

\* E-mail: e.leonova@uva.nl

† NASA Hubble Fellow, Pappalardo Fellow

absorbed by neutral hydrogen in the intergalactic medium, reducing its visibility at high redshift. A dramatic decline in the number of galaxies showing Lyman- $\alpha$  emission was observed between  $z = 6-7$ , suggesting a rapid evolution of the neutral hydrogen fraction in the IGM (Stark et al. 2010, 2017; Pentericci et al. 2011; Mason et al. 2018a; Napolitano et al. 2025). Despite these difficulties, detections of LAEs at even higher redshifts have been reported in several recent studies (Song et al. 2016; Zitrin et al. 2015; Tilvi et al. 2020; Jung et al. 2020; Roberts-Borsani et al. 2023; Saxena et al. 2023; Chen et al. 2024; Tang et al. 2024), with the record being at  $z = 13.0$  (Witstok et al. 2024).

What makes a galaxy a LAE at high redshift? High- $z$  LAEs are thought to be located within ionized bubbles created by neighbouring galaxies, allowing Lyman- $\alpha$  photons to escape before being redshifted and absorbed by the neutral intergalactic medium (e.g., Mason et al. 2018b; Matthee et al. 2018; Napolitano et al. 2024; Chen et al. 2024; Witstok et al. 2024; Tang et al. 2024; Napolitano et al. 2025). These overdense regions contain many galaxies, each contributing to the process of ionization, creating larger ionized regions that allow Lyman- $\alpha$  photons to escape (e.g., Castellano et al. 2018; Jung et al. 2022; Larson et al. 2022; Leonova et al. 2022; Endsley & Stark 2022; Saxena et al. 2023; Tang et al. 2023, 2024; Witten et al. 2024; Chen et al. 2025; Hashemi et al. 2025; Whitler et al. 2025). However, alternative scenarios suggest that individual luminous sources, particularly bright galaxies or AGN, may drive localized ionized bubbles sufficiently large to facilitate Lyman- $\alpha$  transmission (e.g., Matthee et al. 2018; Meyer et al. 2021).

On the other hand, Lyman- $\alpha$  visibility is also shaped by intrinsic galaxy properties, including star formation history, ionizing photon production, and energetic sources such as AGNs. Notably, the Lyman- $\alpha$  escape fraction correlates strongly with dust attenuation (e.g., Atek et al. 2009; Hayes et al. 2011; Martin et al. 2025), suggesting that dust geometry and UV absorption play critical roles in determining whether Lyman- $\alpha$  photons reach the observer. Since dust-free or low-dust systems exhibit enhanced Lyman- $\alpha$  transmission, systematic variations in dust properties across our LAE and non-LAE samples could substantially influence observability independent of environmental factors. Bursty star formation episodes can enhance ionization, potentially creating clearer pathways for Lyman- $\alpha$  photons to escape (Matthee et al. 2017; Begley et al. 2024; Boyett et al. 2024). Other studies suggest that Lyman- $\alpha$  visibility may also be linked to galaxy mergers. Witten et al. (2024) showed that galaxies with frequent mergers can experience periods of intense star formation, leading to strong Lyman- $\alpha$  emission. Additionally, AGN activity could contribute to ionization, further influencing Lyman- $\alpha$  transmission and its detectability at high redshifts (Giallongo et al. 2015; Yung et al. 2021; Dayal et al. 2024). Disentangling the role of these intrinsic properties from environmental factors is a crucial step towards constraining the physics, timeline, and protagonists of reionization (e.g., Finkelstein et al. 2019; Naidu et al. 2020; Matthee et al. 2022; Asthana et al. 2024; Lu et al. 2025).

The launch of the James Webb Space Telescope (JWST) has transformed the study of the Epoch of Reionization (EoR) (Ellis 2025; Stark et al. 2026). The Lyman- $\alpha$  emission lines from EoR galaxies are redshifted into the infrared, and JWST's sensitivity enables the detection of even faint and distant LAEs, providing key data about the state of the universe during the EoR.

Critical to the study of galaxy environments, JWST enables detailed spectroscopic analysis of distant galaxies, providing unprecedented insights into their physical conditions and emission properties (e.g., Covelo-Paz et al. 2024; Herard-Demanche et al. 2025; Matharu et al. 2024; Matthee et al. 2024; Nelson et al. 2024; Xiao et al. 2024;

Witten et al. 2025). Building on these capabilities, wide-area NIRCam grism surveys now allow us to measure the three-dimensional positions of complete galaxy samples for the first time, enabling the identification of large-scale overdensities and ionized bubbles in the reionization-era universe (Chen et al. 2024; Witstok et al. 2024; Tang et al. 2024; Helton et al. 2024; Torralba-Torregrosa et al. 2024; Naidu et al. 2024; Kashino et al. 2025). For example, the [O III] emission line at 5008 Å is a powerful probe of the ionization state and gas-phase metallicity of galaxies, while Balmer recombination lines such as H $\alpha$  and H $\beta$  more directly trace ongoing star formation. Together, these diagnostics provide insights into the ionizing photon output of galaxies and their contribution to reionizing the IGM (Matthee et al. 2023; Begley et al. 2024; Endsley et al. 2021, 2024; Meyer et al. 2024). Additionally, rest-optical lines like [O III] enable the measurement of systemic redshifts, which in turn provide much more reliable measurements on reionization with the use of the Lyman- $\alpha$  emission lines (e.g., Chen et al. 2024; Napolitano et al. 2024; Saxena et al. 2024; Tang et al. 2024). By studying LAEs alongside [O III] emitters, we can examine whether LAEs preferentially reside in over-dense regions of star-forming galaxies, which may contribute to the formation of large ionized bubbles that facilitate Lyman- $\alpha$  escape.

In this paper, we investigate the environments of LAEs during the Epoch of Reionization, focusing on identifying overdensities of [O III] emitters around LAEs using data from the JWST FRESCO program (Oesch et al. 2023; Meyer et al. 2024). Our goal is to understand the mechanisms driving reionization, particularly through the analysis of LAEs and their surrounding environments. In particular, we use the new systemic redshift measurements obtained from the FRESCO grism program in order to search for new Lyman- $\alpha$  emission lines from the large archive of Keck/MOSFIRE data taken over the last decade in the GOODS fields. Using these new LAEs together with JWST/NIRSpec LAEs reported in the literature, we will examine the properties of LAEs at  $z = 7-8$  in GOODS-N and GOODS-S, and focus on the spatial distribution and clustering of [O III] emitters around LAEs.

In Section 2, we describe the observational data used in this work, including a new Keck archival search for LAEs. In Section 3, we present our analysis and results. Sections 4 and 5 summarize our findings. Throughout this paper, we adopt a flat  $\Lambda$ CDM cosmology with parameters from the Planck Collaboration (Planck Collaboration et al. 2020):  $H_0 = 67.4 \text{ km s}^{-1} \text{ Mpc}^{-1}$ ,  $\Omega_m = 0.315$ , and  $\Omega_\Lambda = 0.685$ . All magnitudes are given in the AB system (Oke & Gunn 1983).

## 2 DATA

Understanding the environments of LAEs requires high-quality spectroscopic and imaging data. In this section, we describe the dataset used in this study, which allows us to identify and analyze the distribution of [O III] emitters around LAEs in GOODS-N and GOODS-S fields.

### 2.1 FRESCO [O III] emitters

We use NIRCam/grism data from FRESCO (First Reionization Epoch Spectroscopically Complete Observations; Oesch et al. 2023) to select [O III] emitters in the GOODS-N and GOODS-S fields, focusing on galaxies at  $z > 7$ . FRESCO covers 62 arcmin<sup>2</sup> in each of these fields, providing a total survey area of 124 arcmin<sup>2</sup>.

The NIRCam/grism observations of FRESCO were performed

with the F444W filter, exposing for approximately 2 hours per pointing. These observations, with a resolution of  $R \sim 1600$ , cover the wavelength range of 3.8–5.0  $\mu\text{m}$ , capturing spectra for all galaxies within the NIRC2 field of view. The setup allows for the measurement of critical emission lines across different cosmic epochs, including [OIII] and H $\beta$  for galaxies at redshifts  $\sim 6.8$ –9. In particular, we use the [OIII] emitter sample of 137 galaxies that was previously discussed and published in Meyer et al. (2024). Note that in GOODS-N, our galaxy IDs differ from those in Meyer et al. (2024) as we use an earlier version of the ID catalog.

In addition to the spectroscopic data, FRESCO provides deep, high-resolution imaging in the F182M, F210M, and F444W filters, reaching a depth of  $\sim 28.2$  mag ( $5\sigma$  in 0.32" diameter apertures). This imaging complements the spectral data by facilitating stellar mass estimates and calibrating slit-loss corrections for NIRSpec/MSA spectra in overlapping fields.

Additionally, the FRESCO field is partially covered by the JWST Advanced Deep Extragalactic Survey (JADES) (Eisenstein et al. 2023). JADES offers much deeper imaging and broader wavelength coverage compared to FRESCO, with an average of 130 hours of exposure time spread over 9 NIRC2 filters, covering the spectral range from 0.6 to 5.3  $\mu\text{m}$ , and also provides deep NIRSpec spectroscopy for large galaxy samples in this field (D'Eugenio et al. 2024).

This extensive dataset enables the identification of LAEs over a wide redshift range ( $6.6 \lesssim z \lesssim 9.3$ ) (Saxena et al. 2023; Tang et al. 2024). In this work we focus on the interval  $7 < z < 8$ , which corresponds to the range where Lyman- $\alpha$  falls within the MOSFIRE Y band, providing valuable context and complementing the sample of new LAEs discovered using the FRESCO data.

## 2.2 Lyman- $\alpha$ emitters

To investigate the overdensities around LAEs in the GOODS-N and GOODS-S fields, we will examine all known LAEs at redshifts  $7 < z < 8$  within the FRESCO field both from ground-based Keck data (e.g., Jung et al. 2022) as well as from new NIRSpec observations (e.g., Saxena et al. 2024). Additionally, we search for new LAEs in archival ground-based Keck/MOSFIRE data.

Since the GOODS fields have been studied extensively over the past decades, in particular in the search for high-redshift galaxy candidates, these fields have been covered with a large amount of Keck/MOSFIRE spectroscopy in the NIR. The main purpose of these observations was often to target the redshifted Lyman- $\alpha$  line. While reliably detecting faint Lyman- $\alpha$  can be challenging due to the NIR sky, we can now leverage FRESCO spectroscopic data, to accurately determine the redshifts of [OIII] emitters to discover new LAEs. Knowing the [OIII] redshifts of galaxies is crucial, as it allows us to revisit ground-based archival data to search for Lyman- $\alpha$  lines at these redshifts.

We utilize archival Keck MOSFIRE data made available via the grizli-Keck archive<sup>1</sup> that has previously been used in Valentino et al. (2022) and includes reductions of MOSFIRE data up to 2022. Among the 71 FRESCO [OIII] emitters at  $z \sim 7$ –8 in GOODS-N, 24 have existing Keck/MOSFIRE data in the Lyman- $\alpha$  wavelength range. Of these, 10 exhibit a Lyman- $\alpha$  line, allowing us to identify 8 new LAEs in the GOODS-N field (Table 1). These include GN\_27795 (N107M, 2014A, PI: Finkelstein), GN\_26844 (N100M, 2013A, PI: Finkelstein), GN\_4394 (U076M, 2014A, PI: Faber), GN\_8563 (N118, 2022A, PI: Casey, Nunez, Prusinski, Steidel), GN\_29193 (N100M,

2013A, PI: Finkelstein), GN\_14535 (U092M, 2016A, PI: Faber, Guo, Yesuf, Koo, Barro), GN\_9680 (C194M, 2013A, PI: Konidaris), and GN\_25604 (N107M, 2014A, PI: Finkelstein). In addition to these, we include four previously known LAEs in GOODS-N (GN\_26051, GN\_22679, GN\_29192, and GN\_19441) identified in earlier studies (Jung et al. 2020; Saxena et al. 2023; Tang et al. 2024).

In the GOODS-S field, 13 out of 40 FRESCO [OIII] emitters have Keck/MOSFIRE coverage in the Lyman- $\alpha$  wavelength range. Among these, we detect Lyman- $\alpha$  emission in three galaxies: GS\_1744, GS\_6644, and GS\_28631, all previously identified in the literature (Song et al. 2016; Roberts-Borsani et al. 2023; Saxena et al. 2023; Tang et al. 2024). We also include the previously confirmed LAE JADES-13682 in our analysis (Tang et al. 2024).

We extracted the Lyman- $\alpha$  emission spectra from the 1D and 2D spectra files associated with each target in our sample. For the flux calibration, we used slit stars observed within the same mask as the potential LAEs. We determined the best stellar fit using model stellar spectra from Castelli & Kurucz (2003), along with Gaia (Gaia Collaboration et al. 2023) photometric magnitudes and astrophysical parameters (effective temperature, surface gravity, and metallicity). We then flux- and slit-corrected the galaxy spectra using the standard star spectra. For each source, we selected LAEs by requiring a signal-to-noise ratio ( $\sigma$ ) greater than 5 in the Lyman- $\alpha$  line to ensure reliable detection. Each target file was loaded and aligned with its redshift-corrected wavelength grid based on the Lyman- $\alpha$  rest-frame wavelength of 1215.67 Å. To analyze the Lyman- $\alpha$  emission in our sample of LAEs, we applied a Bayesian approach to model the observed 1D spectra. We modeled the Lyman- $\alpha$  line profile with a Gaussian function, using the known [OIII] redshift to inform our initial estimate for the line center. Since the redshift is determined from the [OIII] line, we have an approximate expected wavelength for the Lyman- $\alpha$  emission.

To determine the velocity offset ( $\Delta v$ ) between the Lyman- $\alpha$  and [OIII] emission lines, we use the formula:

$$\Delta v = c \frac{(z_{\text{Ly}\alpha} - z_{\text{[OIII]}})}{(1 + (z_{\text{Ly}\alpha} + z_{\text{[OIII]}})/2)}, \quad (1)$$

where  $z_{\text{Ly}\alpha}$  is a Lyman- $\alpha$  redshift,  $z_{\text{[OIII]}}$  is [OIII] redshift, and  $c$  is the speed of light. We applied a Gaussian fitting approach combined with bootstrapping to estimate uncertainties. For each source, we perturbed the [OIII] redshift by random variations within 60 km/s to simulate observational uncertainties. For each perturbed redshift, we ran an MCMC sampler to obtain the Lyman- $\alpha$  redshift. This process was repeated 1000 times to generate a distribution of velocity offsets. From this sample, we calculated the mean velocity offset and its uncertainty, reported as the 16th and 84th percentiles, which account for both intrinsic and observational variations in the velocity offset measurements. For fitting the Lyman- $\alpha$  line parameters, we used a Markov Chain Monte Carlo (MCMC) sampler to explore the posterior distribution and maximize the likelihood function, accounting for uncertainties and potential asymmetry in parameter distributions.

The 2D spectra shown in Fig. 1 were normalized, clipped, and smoothed using a Gaussian filter to emphasize the Lyman- $\alpha$  line region for each target. For visualization, we used a dual-panel format, where the smoothed and resampled 1D spectra are displayed below the processed 2D image, both centered around the Lyman- $\alpha$  emission line (Figure 1).

In Table 1 we list the LAEs identified in the GOODS-S and GOODS-N fields. The  $z_{\text{Ly}\alpha}$ ,  $z_{\text{[OIII]}}$  and Lyman- $\alpha$  flux ( $F_{\text{Ly}\alpha}$ ) in  $\text{erg s}^{-1} \text{cm}^{-2}$  for each target are provided, along with the corresponding

<sup>1</sup> <https://grizli-cutout.herokuapp.com/mosfire?mode=table>

ID	RA	DEC	$z_{\text{Ly}\alpha}$	$z_{\text{[OIII]}}$	$\Delta v$ [km s <sup>-1</sup> ]	$F_{\text{Ly}\alpha}$ [10 <sup>-17</sup> erg s <sup>-1</sup> cm <sup>-2</sup> ]	$\text{EW}_{\text{Ly}\alpha}$ [Å]	Instrument	References
<b>GN LAEs</b>									
GN_27795	189.13498	62.29190	7.038	7.017	792 <sup>+36</sup> <sub>-37</sub>	3.10 ± 0.91	151 ± 17	Keck MOSFIRE <sup>1</sup>	
GN_26051	189.17981	62.28239	7.087	7.084	122 ± 53 <sup>a</sup>	-	52 ± 9 <sup>a</sup>	JWST NIRSPEC	a
GN_22679	189.20377	62.26843	7.090	7.090	233 ± 53 <sup>a</sup>	1.61 ± 0.09 <sup>a</sup>	143 ± 8 <sup>a</sup>	JWST NIRSPEC	a
GN_4394	189.08349	62.20258	7.197	7.186	398 <sup>+34</sup> <sub>-29</sub>	3.80 ± 0.48	221 ± 15	Keck MOSFIRE <sup>3</sup>	
GN_26844	189.22512	62.28629	7.211	7.205	168 <sup>+41</sup> <sub>-36</sub>	0.79 ± 0.02	54 ± 5	Keck MOSFIRE <sup>2</sup>	
GN_8563	189.08405	62.22204	7.206	7.200	236 <sup>+45</sup> <sub>-43</sub>	1.74 ± 0.22	51 ± 2	Keck MOSFIRE <sup>4</sup>	
GN_29192	189.15779	62.30234	7.507	7.498	314 <sup>+43</sup> <sub>-42</sub>	2.07 ± 0.09	72 ± 4	Keck MOSFIRE <sup>1</sup>	b
GN_29193	189.15798	62.30240	7.507	7.502	171 <sup>+41</sup> <sub>-42</sub>	1.06 ± 0.02	27 ± 1	Keck MOSFIRE <sup>2</sup>	
GN_19441	189.33307	62.25722	7.600	7.595	161 <sup>+40</sup> <sub>-37</sub>	1.90 ± 0.05	46 ± 3	Keck MOSFIRE <sup>6</sup>	b
GN_9680	189.28867	62.22651	7.636	7.629	235 <sup>+35</sup> <sub>-38</sub>	1.86 ± 0.04	143 ± 6	Keck MOSFIRE <sup>7</sup>	
GN_14535	189.20307	62.24249	7.657	7.648	315 <sup>+40</sup> <sub>-38</sub>	1.56 ± 0.03	86 ± 10	Keck MOSFIRE <sup>5</sup>	
GN_25604	189.30014	62.28034	7.700	7.694	226 <sup>+44</sup> <sub>-38</sub>	2.86 ± 0.08	241 ± 47	Keck MOSFIRE <sup>1</sup>	
<b>GS LAEs</b>									
GS_1744	53.16958	-27.73806	7.242	7.242	269 ± 94 <sup>a</sup>	0.48 ± 0.07 <sup>a</sup>	26 ± 3 <sup>a</sup>	JWST NIRSPEC	a
JADES-13682	53.16745	-27.77203	7.275	-	217 ± 93 <sup>a</sup>	0.23 ± 0.03 <sup>c</sup>	259 ± 54 <sup>a</sup>	JWST NIRSPEC	a, c
GS_6644	53.13347	-27.76039	7.660	7.661	277 ± 89 <sup>a</sup>	0.55 ± 0.09 <sup>d</sup>	33 ± 3 <sup>a</sup>	JWST NIRSPEC	a, d
GS_28631	53.08733	-27.86028	7.962	7.958	327 ± 65 <sup>c</sup>	0.24 ± 0.08 <sup>e</sup>	16 ± 8 <sup>e</sup>	JWST NIRSPEC	e

**Notes:**

[1] N107M, 2014A, PI: Finkelstein; [2] N100M, 2013A, PI: Finkelstein; [3] U076M, 2014A, PI: Faber; [4] N118, 2022A, PI: Casey, Nunez, Prusinski, Steidel; [5] U092M, 2016A, PI: Faber, Guo, Yesuf, Koo, Barro; [6] U085M, 2015A, PI: Faber; [7] C194M, 2013A, PI: Konidaris

**References:** [a] Tang et al. (2024); [b] Jung et al. (2020); [c] Saxena et al. (2023); [d] Song et al. (2016); [e] Roberts-Borsani et al. (2023)

**Table 1.** Table of Lyman- $\alpha$  Emitters in GOODS-S and GOODS-N fields, including coordinates, redshifts, velocity offsets, instruments used, and relevant references. The sample is restricted to sources with a signal-to-noise ratio (SNR) greater than 5 in the Lyman- $\alpha$  emission, ensuring reliable detection.

velocity offset ( $\Delta v$ ) in km s<sup>-1</sup> which reflects the difference between the Lyman- $\alpha$  and [OIII] redshifts.

Out of 71 [OIII] emitters in GOODS-N and 40 [OIII] emitters in GOODS-S, we find that the fraction of LAEs (only including LAEs with  $\text{EW} > 25$  Å) among galaxies with  $M_{\text{UV}} \leq -19.5$  at  $7 < z < 8$  is  $0.28 \pm 0.07$  in GOODS-N and  $0.08 \pm 0.05$  in GOODS-S. Combined, the overall LAE fraction in the GOODS fields is  $0.19 \pm 0.05$ .

It is important to note that the Lyman- $\alpha$  line was not detected in the Keck data for some [OIII] emitters, and certain emitters were outside the coverage of Keck or JWST observations within the Lyman- $\alpha$  wavelength range. Therefore, the LAE fractions reported above should be considered as lower limits, since we cannot definitively rule out the possibility that these [OIII] emitters are also LAEs

### 3 RESULTS

In this section, we analyze the spatial distribution, clustering properties, and intrinsic characteristics of [OIII] emitters and LAEs at  $7 < z < 8$ . We first identify and categorize groups of LAEs in GOODS-N and GOODS-S to explore their large-scale environments. We then investigate the relationship between Lyman- $\alpha$  visibility and galaxy overdensities, comparing the environments of LAEs to those of non-LAE [OIII] emitters. Additionally, we examine the intrinsic properties of these galaxies, including their UV magnitudes,  $\beta$  slopes, stellar masses, and [OIII] equivalent widths, to assess the factors influencing Lyman- $\alpha$  emission.

By combining environmental and intrinsic analyses, we aim to understand how both factors contribute to Lyman- $\alpha$  visibility and which plays a more dominant role.

#### 3.1 Groups of LAEs

To investigate the environment of LAEs at  $7 < z < 8$ , we categorized the galaxies into four groups in GOODS-N (Figure 2) and three groups in GOODS-S (Figure 3). Each group spans 30 cMpc and is centered around the brightest LAE or one of the brightest in the region. This approach minimizes overlap between groups, allowing us to analyze distinct spatial regions independently.

In many studies at  $7 < z < 8$  the typical size of ionized bubbles surrounding LAEs is estimated to be 0.5-1 pMpc (Hayes & Scarlata 2023; Umeda et al. 2024; Witstok et al. 2024; Napolitano et al. 2024). However, LAEs are expected to form within larger-scale overdensities, where multiple ionized regions may merge into extended structures. By using a 30 cMpc grouping scale, we aim to capture the broader cosmic environment of LAEs. Additionally, a 30 cMpc scale ensures that we analyze distinct spatial regions while minimizing overlap, helping us distinguish environmental differences between groups.

Each group and its corresponding LAE are represented by different colors for visual clarity. The naming of the groups was based on the redshift of the central LAE in each region: GN\_z7\_0, GN\_z7\_2, GN\_z7\_5, GN\_z7\_6, GS\_z7\_2, GS\_z7\_7, and GS\_z8. This classification allows for a systematic investigation of the local environment and clustering properties of LAEs in the GOODS-N and GOODS-S fields, particularly focusing on the ionized regions around them at redshifts 7 to 8. The individual [OIII] and H $\beta$  grism spectra and tables of all sources in each group are presented in the appendix.



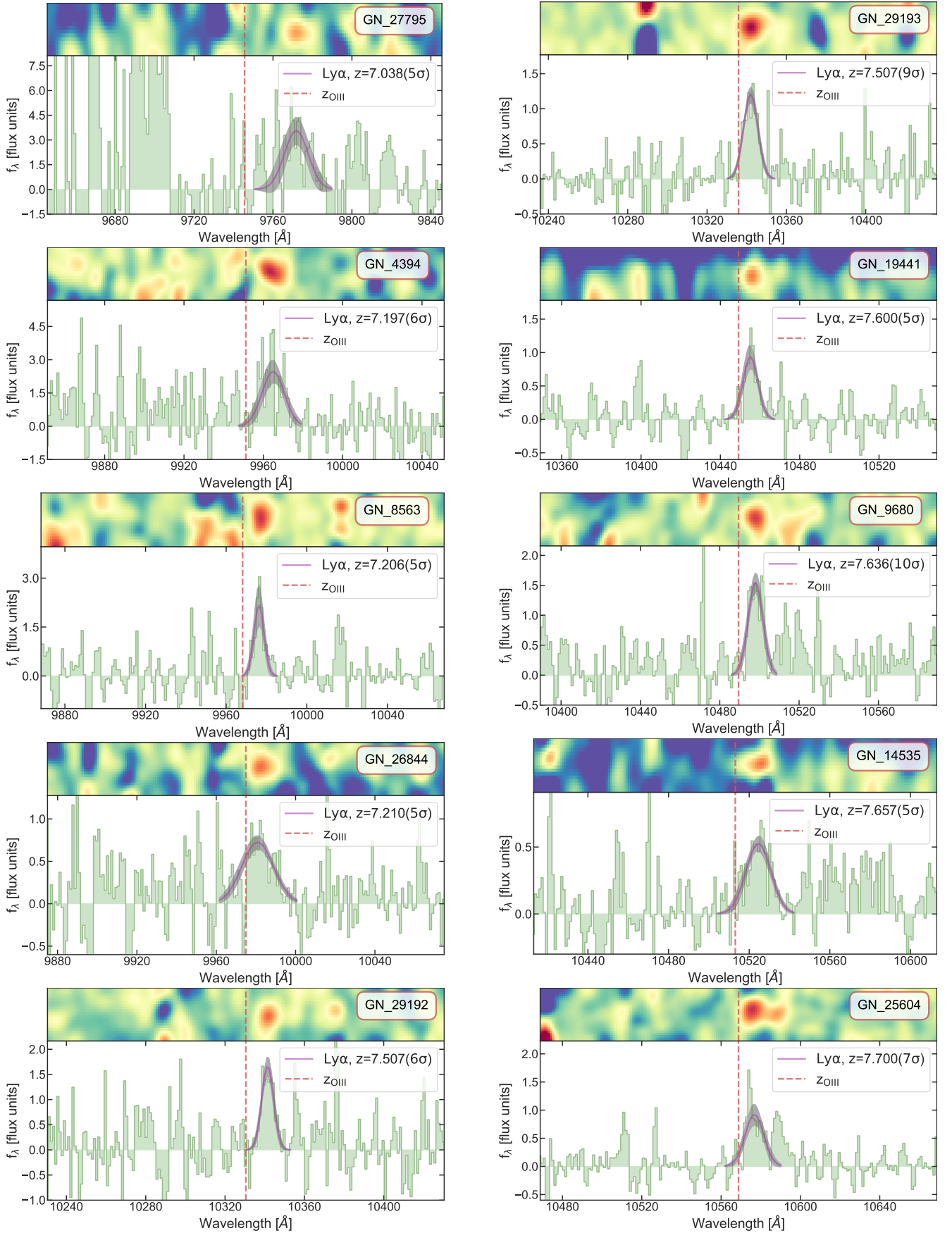


**Figure 1.** Spectra of Lyman- $\alpha$  emission for LAEs in the GOODS-N field. The top panel presents the 2D signal-to-noise spectra obtained using Keck MOSFIRE (Table 1), with each plot centered around the Lyman- $\alpha$  emission line. The dotted vertical line indicates the expected rest-frame Lyman- $\alpha$  position based on [OIII] redshift measurements. The bottom panel shows the corresponding 1D spectra, fitted with Gaussian profiles to model Lyman- $\alpha$  emission line.

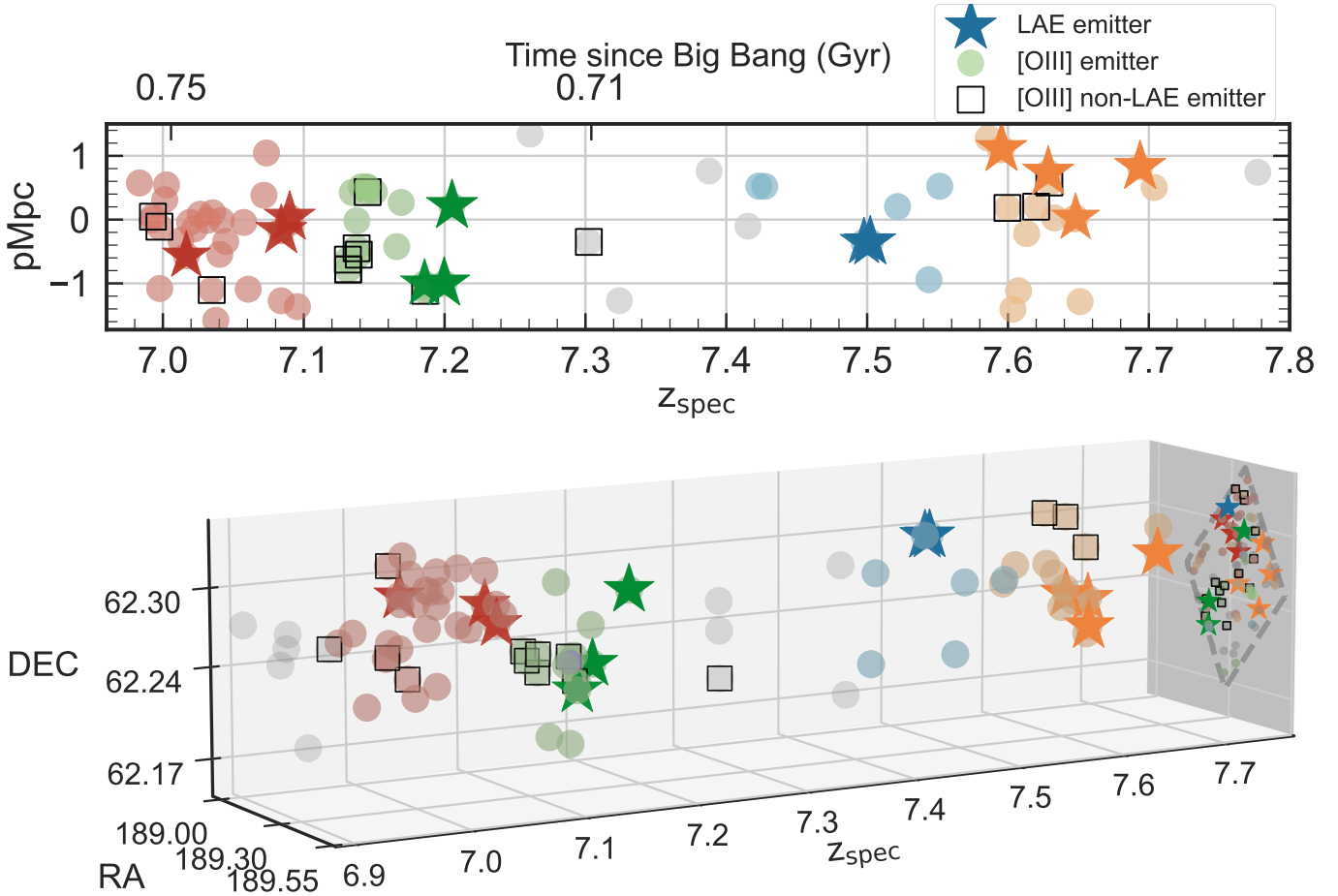


**Figure 2.** The spatial distribution of Lyman- $\alpha$  and [OIII] emitters in GOODS-N is shown through 2D (top panel) and 3D (bottom panel) projections. The galaxies in the FRESCO field in GOODS-N are organized into four groups, each spanning 30 cMpc, with each group centered around the brightest LAE or one of the brightest galaxies in the region. Circles represent [OIII] emitters, stars indicate LAEs, and black squares highlight [OIII] emitters with spectra in the Keck archive at the Lyman  $\alpha$  wavelength that were not detected as LAEs. The color scheme highlights the LAEs and their companions within each group: red for GN\_z7\_0, green for GN\_z7\_2, blue for GN\_z7\_5, and orange for GN\_z7\_6.

### 3.1.1 GOODS-N

In the GOODS-N field, the first group, **GN\_z7\_0** (Figure A1, Table A1), centered at redshift  $z \sim 7$ , consists of **30 [OIII] emitters**, including **3 LAEs**: GN\_27795, GN\_26051, and GN\_22679. On Figure 2, this group is represented by red circles, and the LAEs are marked as red stars. This is the most populated group in our study. It includes several luminous galaxies with  $M_{UV} < -20$  and massive galaxies, GN\_14967 and GN\_30464, with  $\log_{M_{\star}} > 9.25$ . GN\_26051 and GN\_22679 were first identified in Tang et al. (2024), where the large overdensity at this redshift around these sources was discovered.

The second group, **GN\_z7\_2** (Figure A2, Table A2), is situated at  $z \sim 7.2$  and contains **17 [OIII] emitters**, depicted as green circles in Figure 2. Among these, **3 are LAEs**—GN\_4394, GN\_8563, and GN\_26844—highlighted as green stars. This group houses exceptionally luminous galaxies, and also features extraordinarily bright AGN, such as GN\_5688 (GNz7q; Fujimoto et al. 2022).

Another candidate, GN\_14101, previously identified in (Jung et al. 2020) as z8\_GND\_22233, was reported to have an emission line at  $1.015 \mu\text{m}$  with  $S/N = 7.1$ . At a redshift of  $z = 7.145$ , this corresponds to the NV line. This raises the possibility that GN\_14101 could also host AGN activity, bringing the total number of AGNs in this group to three, including one AGN that is also an LAE. An interesting

feature of the group GN\_z7\_2 is the presence of GN\_26844, an LAE, which is accompanied by another LAE, GN\_4394, that stands out due to its exceptionally large Lyman- $\alpha$  equivalent width of  $221 \text{ \AA}$ . This unusually high EW of Lyman- $\alpha$ , combined with a broad H $\beta$  line with  $\text{FWHM} = 1069 \pm 239 \text{ km/s}$  (Xiao et al. 2025), raises the possibility that GN\_4394 may also be an AGN. Notably, it is located just  $0.167 \text{ pMpc}$  from GN\_5688. The potential presence of an AGN in this context highlights the need for deeper investigation into the interactions between LAEs and AGNs, especially regarding their contributions to ionization and the overall evolution of the group.

The third group, **GN\_z7\_5** (Figure A3, Table A3), at  $z \sim 7.5$ , includes **7 companions** (blue circles), and **two LAEs**, GN\_29192 and GN\_29193, marked by blue stars. These two LAEs are very close to each other, suggesting a potential merger, which might explain the Lyman- $\alpha$  emission.

Finally, the group **GN\_z7\_6** (Figure A4, Table A4), consisting of **16 sources** (orange circles), includes **4 LAEs**: GN\_19441, GN\_14535, GN\_25604, and GN\_9680, marked by orange stars.

Interestingly, there is a significant clustering of bright galaxies in the GN\_z7\_0 group, which is not observed between the GN\_z7\_2 and GN\_z7\_5 groups. Bright galaxies appear to reside in the most overdense region and may serve as tracers of large-scale structure.

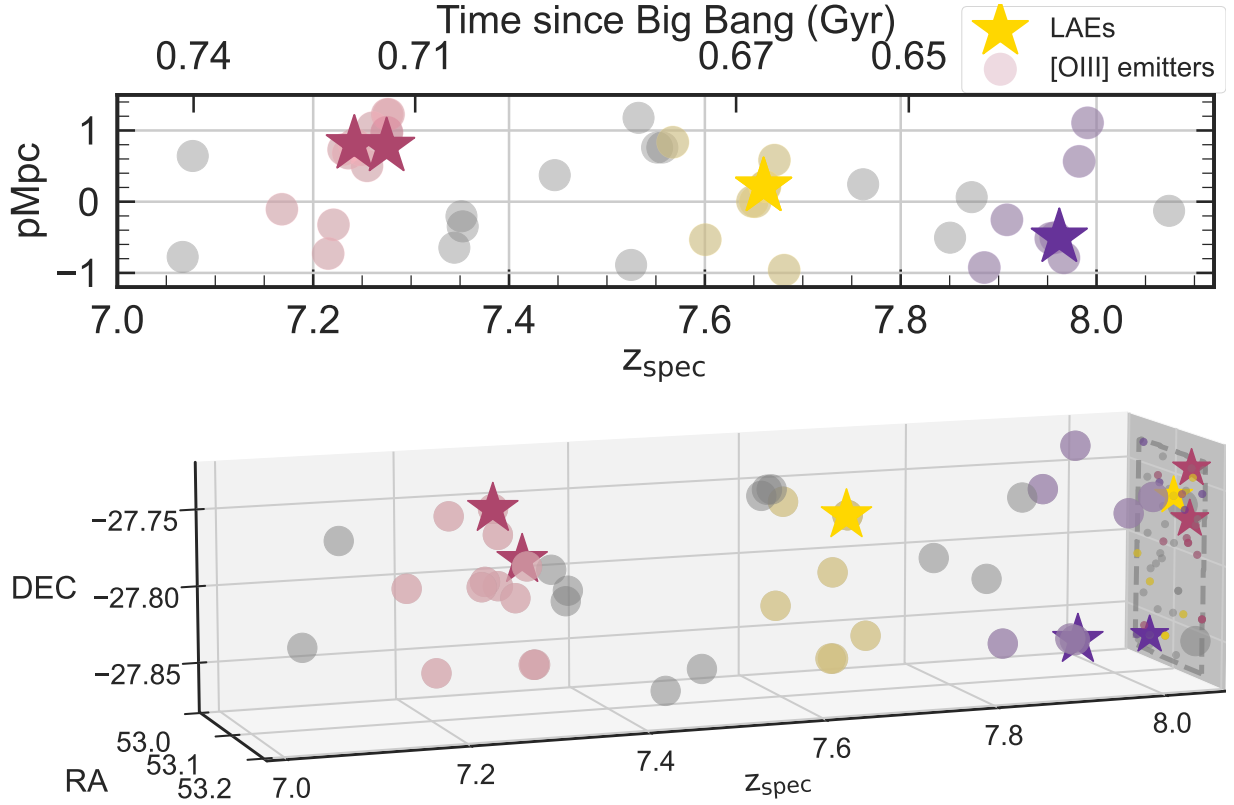


**Figure 3.** The spatial distribution of Lyman- $\alpha$  and [OIII] emitters in GOODS-S is shown through 2D (top panel) and 3D (bottom panel) projections. The galaxies in the FRESCO field in GOODS-S are organized into three groups, each spanning 30 cMpc, with each group centered around the brightest LAE or one of the brightest galaxies in the region. Circles represent the [OIII] emitters, while stars indicate the LAEs. The color scheme highlights the LAEs and their companions within each group: pink for GS\_z7\_2, yellow for GS\_z7\_7, and purple for GS\_z7\_8.

### 3.1.2 GOODS-S

The first group in the GOODS-S field, **GS\_z7\_2** (Figure A5, Table A5), with a redshift of  $z \sim 7.2$ , consists of **12 [OIII] emitters**, represented in Figure 3 as pink circles, including 2 LAEs: GN\_1744 and JADES-13682. One of the LAEs, JADES-13682, identified in (Saxena et al. 2023), is very faint and is not detected as an [OIII] emitter in FRESCO. The overdensity around this LAE and the presence of bright companions in its vicinity may explain the visibility of Lyman- $\alpha$  line and for such a faint source. The overdensity around JADES-13682 was also confirmed in Helton et al. (2024); Endsley et al. (2024); Tang et al. (2024); Witstok et al. (2024); Chen et al. (2025).

Another group in GOODS-S, **GS\_z7\_7** (Figure A6, Table A6), marked as yellow, located around the bright LAE GS\_6644, previously identified by Song et al. (2016), consists of only **7 companions** within 30 cMpc. One of the companions, GS\_6645, is in very close proximity to LAE GS\_6644. Their close location and matching redshift suggest that these two galaxies might be undergoing a merger process.

The final group in GOODS-S, **GS\_z8** (Figure A7, Table A7), is centered around LAE GS\_28631, previously identified by Roberts-Borsani et al. (2023) at  $z \sim 8$ . This group, marked as purple, includes **7 [OIII] emitters**.

The local environment in GOODS-S shows slightly different clustering properties compared to GOODS-N, potentially indicative of varied large-scale structure at  $z \sim 7-8$ . The density of bright [OIII] emitters ( $M_{UV} < -19.5$ ) in GOODS-S are lower compared to that in

GOODS-N, suggesting that fainter sources dominate the population in this field.

### 3.2 Overdensities around LAEs

The spatial distribution of galaxies can play a crucial role in shaping their visibility and the formation of ionized bubbles during reionization. LAEs are often found in overdense regions, where neighboring galaxies may help create ionized bubbles that facilitate Lyman- $\alpha$  escape (Castellano et al. 2018; Jung et al. 2022; Larson et al. 2022; Leonova et al. 2022; Endsley & Stark 2022; Saxena et al. 2023; Tang et al. 2023, 2024; Witten et al. 2024). To test this hypothesis, we compare the overdensities around LAEs with those of [OIII] emitters that do not exhibit detected Lyman- $\alpha$  emission.

To estimate the number of galaxies expected within a given area, we use the UV luminosity function (LF) derived in (Bouwens et al. 2021) at redshifts  $z \sim 2-10$ :

$$\begin{cases} M_{UV}^* = -21.03 - 0.04(z - 6) \\ \phi^*/\text{Mpc}^{-3} = 0.4 \times 10^{-3} \times 10^{-0.33(z-6) - 0.24(z-6)^2} \\ \alpha = -1.94 - 0.11(z - 6) \end{cases} \quad (2)$$

To compute the expected number of detections within the certain volume, we integrate the UV LF as follows:

$$N_{\text{exp}} = \int \Omega \frac{dV_{\text{com}}}{dz} dz \int \phi(M) dM \quad (3)$$

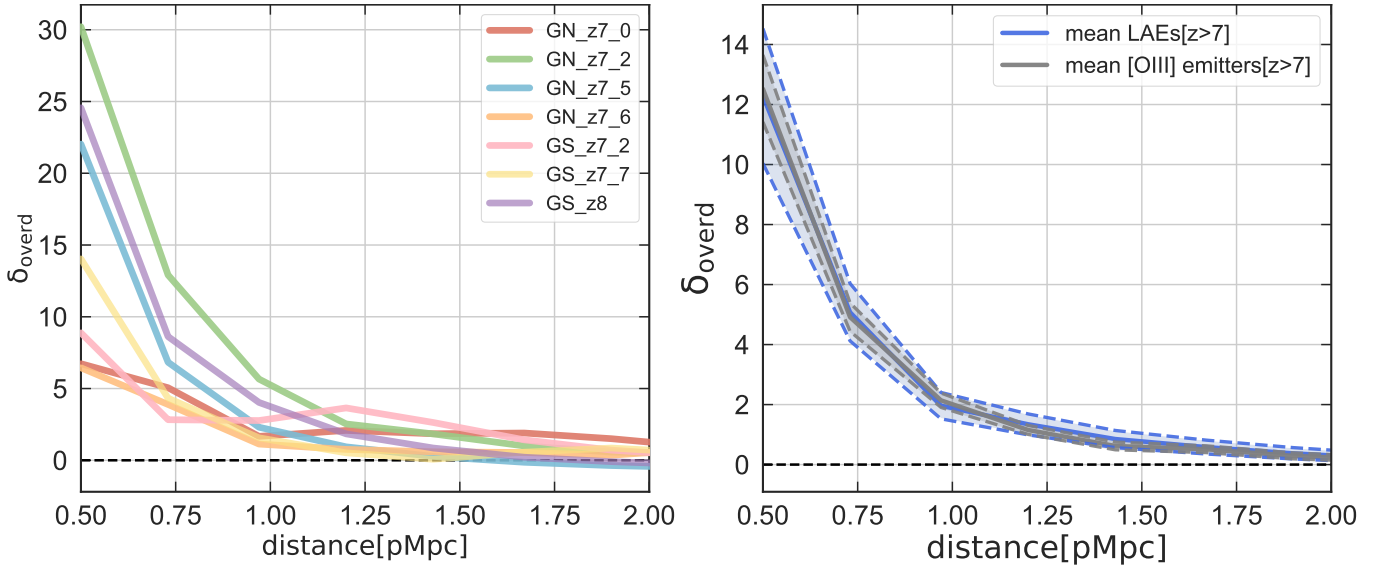


**Figure 4.** **Left panel:** The overdensities around the 7 central LAEs in each group within the GOODS-N and GOODS-S fields. Each curve is color-coded according to the same group scheme as in Figures 2 and 3: red for GN\_z7\_0, green for GN\_z7\_2, blue for GN\_z7\_5, orange for GN\_z7\_6, pink for GS\_z7\_2, yellow for GS\_z7\_7, and purple for GS\_z7\_8. The overdensity parameter is calculated for sources with  $M_{\text{UV}} < -19.5$  to ensure completeness. **Right panel:** The mean overdensity for LAEs across all groups is represented by the blue curve, with the shaded region denoting the 16th to 84th percentile range. The gray line shows the overdensity for [OIII]-non LAEs in the GOODS-N and GOODS-S fields at  $7 < z < 8$ .

We define the overdensity parameter  $\delta$  as the difference between the number of companions and LAEs within 30 cMpc and the expected number of galaxies, normalized by the expected number of galaxies for each group:

$$\delta_{\text{overd}} = \frac{N_{\text{det}} - N_{\text{exp}}}{N_{\text{exp}}} \quad (4)$$

where  $N_{\text{det}}$  is the number of sources detected by the JWST FRESCO survey within the specified distance 1-2 pMpc (or  $\Delta z \sim 0.03 - 0.05$ ) from the central LAE, and  $N_{\text{exp}}$  is the expected number of sources derived from the UV luminosity function (LF) at the relevant redshift. Only sources with  $M_{\text{UV}} < -19.5$  are considered for the overdensity calculation for completeness (Meyer et al. 2024).

A key question in understanding Lyman- $\alpha$  visibility is whether overdense regions, where large ionized bubbles could enhance the transmission of Lyman- $\alpha$  photons, are the primary factor influencing the visibility of LAEs. To test this, we compare the overdensities of LAEs with [OIII]-non LAEs. If overdensity alone determined Lyman- $\alpha$  visibility, we would expect LAEs to reside in significantly higher-density regions.

The left panel of Figure 4 shows the overdensity parameter for each group, with different colors corresponding to different regions. The right panel presents the mean overdensity across all seven groups, shown as a blue curve, with the shaded region representing the 16th–84th percentile range from bootstrap resamplings of individual galaxies. For comparison, the gray dashed curve represents the mean overdensity around all [OIII]-non LAEs in the GOODS-N and GOODS-S fields at  $7 < z < 8$ .

Surprisingly, we find that the mean overdensity parameters are similar for both LAEs and non-LAEs. This suggests that while LAEs have large  $\delta$ , overdensity alone does not determine whether a galaxy exhibits Lyman- $\alpha$  emission. Other factors, such as the presence of sufficiently large ionized bubbles or galaxy properties affecting Lyman- $\alpha$  escape, likely play a role in shaping their visibility.

### 3.3 Properties of [OIII] emitters and LAEs

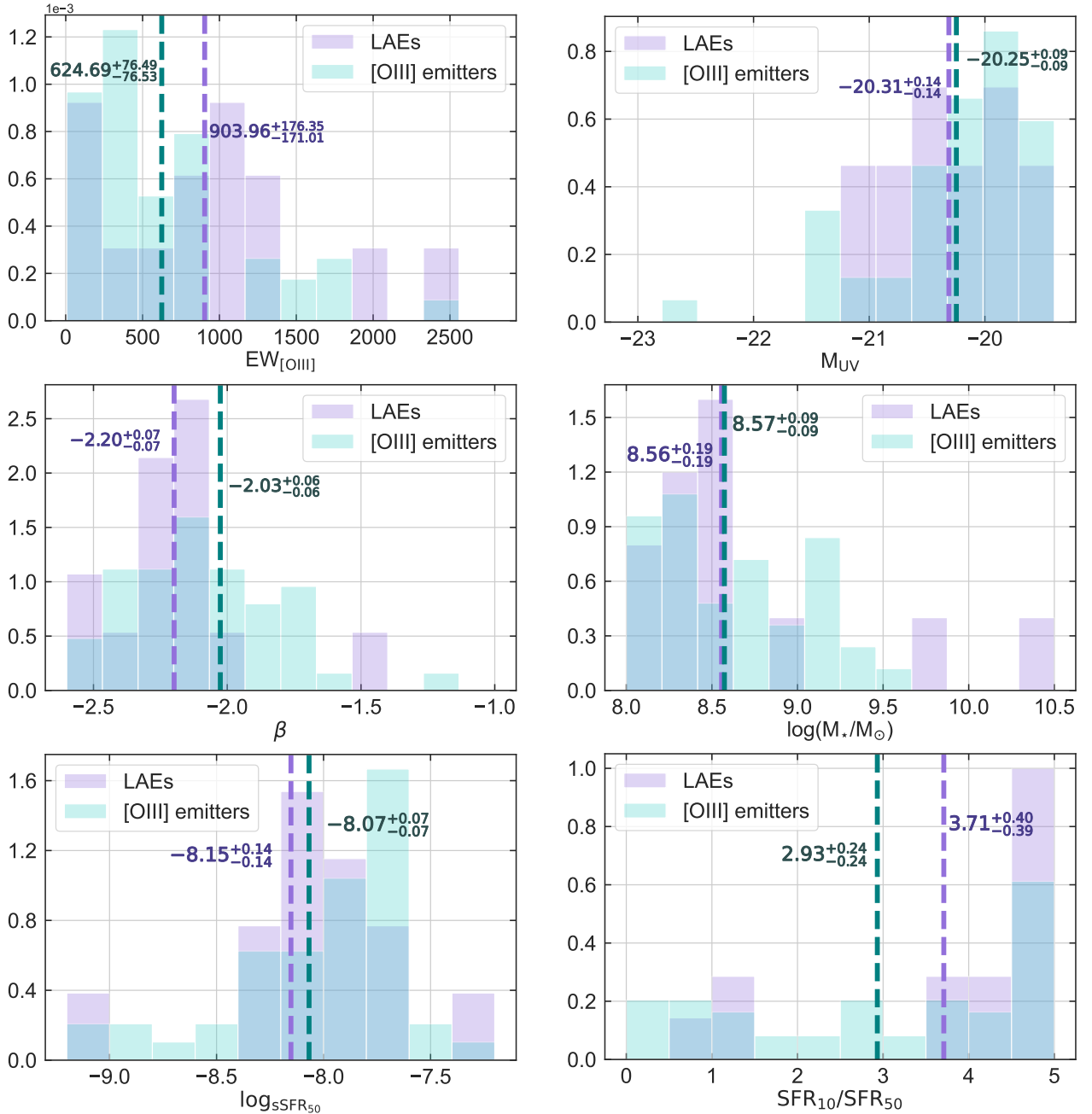
In the previous subsection, we examined the role of large-scale environment in determining Lyman- $\alpha$  visibility by comparing the overdensities of LAEs and non-LAEs. As we have found that overdensities do not correlate with the presence of Lyman- $\alpha$  emission, other physical properties of galaxies must play an important role. In this section, we compare the intrinsic properties of LAEs and other [OIII] emitter, including their  $\beta$  slope, UV magnitude,  $\log M_{\star}$ , EW, and star-formation history, and quantify differences with two-sample K-S tests (Kolmogorov & Smirnov 1933; Virtanen et al. 2020). These quantities are derived using the prospector SED-fitting code (Johnson et al. 2021) following the choices outlined in Naidu et al. (2024).

Figure 5 presents these comparisons, with 14 LAEs shown as purple bars and 49 non-LAE [OIII] emitters as green bars. The mean values for each property are marked by dashed lines. To ensure a fair comparison, we only include sources with magnitudes brighter than  $-19.5$ .

The mean EW of [OIII] for LAEs is higher than that of non-LAE [OIII] emitters ( $D = 0.40$ ,  $p = 0.049$ ), which may indicate a more active star-forming environment or potentially stronger ionizing radiation associated with LAEs. Additionally, the mean star formation rate ratio ( $\text{SFR}_{10}/\text{SFR}_{50}$ ) for LAEs is also slightly elevated compared to [OIII] emitters ( $D = 0.30$ ,  $p = 0.25$ ), suggesting that LAEs may be undergoing more recent or enhanced star formation over the considered timescales.

The UV slopes also shows difference (bluer  $\beta$  for LAEs;  $D = 0.39$ ,  $p = 0.06$ ), suggestive of lower dust content among LAEs. The bluer  $\beta$  slopes of LAEs point to lower dust content, consistent with the known connection between dust attenuation and Lyman- $\alpha$  escape (e.g. Atek et al. 2009; Hayes et al. 2011). The lack of significant differences in  $M_{\text{UV}}$  ( $D = 0.24$ ,  $p = 0.52$ ) and  $\log M_{\star}$  ( $D = 0.21$ ,  $p = 0.64$ ) indicates that luminosity and stellar mass alone are unlikely to fully account for the presence of Lyman- $\alpha$  emission.





**Figure 5.** Properties of [OIII] emitters (green bars) and LAEs (purple bars): This comparison includes several key intrinsic properties, such as the [OIII] EW,  $M_{UV}$ ,  $\beta$  slope, stellar mass ( $\log M_*$ ),  $\log SFR_{10}$ , and  $SFR_{10}/SFR_{50}$ . The green and purple dashed lines represent the mean values for [OIII] and Lyman- $\alpha$  emitters, respectively. The numbers near each line indicate the mean value for each property, with error bars showing the 16th to 84th percentile range.

#### 4 DISCUSSION

The study of LAEs at high redshifts ( $7 < z < 8$ ) in the GOODS-N and GOODS-S fields has provided insights into their spatial distribution, intrinsic properties, and environmental contexts. We compare LAEs with [OIII] emitters that do not show Lyman- $\alpha$  emission to understand how environmental and intrinsic factors affect Lyman- $\alpha$  visibility (e.g. Tang et al. 2024; Witstok et al. 2024; Chen et al. 2025).

Our analysis indicates that LAEs and [OIII] emitters without detected Lyman- $\alpha$  emission exhibit similar mean overdensity parameters, suggesting that in GOODS-N and GOODS-S fields environmental factors do not determine whether a galaxy appears as an LAE. It is

also important to note that for some [OIII] emitters, we did not detect the Lyman- $\alpha$  line in the Keck data, and some were not observed by Keck or JWST within the Lyman- $\alpha$  wavelength range, meaning we cannot definitively conclude that these [OIII] emitters are not LAEs. These sources are therefore treated as non-LAE [OIII] emitters in our analysis.

While our LAEs do not appear significantly more likely to reside in overdense regions compared to non-LAEs, this may partly reflect the adopted Lyman- $\alpha$  EW threshold used to define the sample. In this work, we include all sources with detected Lyman- $\alpha$  emission, spanning a wide range of rest-frame EWs from  $\sim 25$  Å to  $\sim 250$  Å. In contrast, Chen et al. (2025) focus on the most extreme emitters

( $EW > 100 \text{ \AA}$ ) and report that these LAEs are preferentially located in overdense regions, likely tracing large ionized bubbles. Indeed, several of our strongest emitters (e.g. GN\_27795, GN\_4394, GN\_25604, and JADES-13682) fall within this regime, but the inclusion of low- and moderate-EW systems likely makes any link between Lyman- $\alpha$  strength and environment less apparent. Adopting a higher EW threshold in our analysis could therefore reveal a stronger dependence of Lyman- $\alpha$  visibility on environment, since very high-EW emission is expected to occur predominantly in ionized regions with reduced IGM attenuation.

The intrinsic properties of LAEs and other [OIII] emitters provide additional insight into the conditions that influence Lyman- $\alpha$  visibility. Our comparison shows that the EW of [OIII] for LAEs is higher on average than for non-LAE [OIII] emitters, and the mean  $SFR_{10}/SFR_{50}$  ratio is also slightly elevated, suggesting that LAEs may experience more recent or enhanced star formation activity. In contrast,  $M_{UV}$  ( $D = 0.24$ ,  $p = 0.52$ ) and  $\log_{M_\star}$  ( $D = 0.21$ ,  $p = 0.64$ ) show no significant differences between the two populations. The  $\beta$  slopes are bluer for LAEs ( $D = 0.39$ ,  $p = 0.06$ ), consistent with lower dust content and enhanced Lyman- $\alpha$  escape. Overall, these results indicate that Lyman- $\alpha$  visibility is not governed by a single intrinsic property, but likely arises from a combination of factors including dust attenuation, ionization conditions, and local IGM transmission.

The spatial distribution of bright galaxies provides clues about large-scale structure during reionization. In some cases (e.g. GN\_z7\_0), we find significant clustering of luminous sources, consistent with bright galaxies tracing overdense regions (e.g. Endsley et al. 2024; Naidu et al. 2024; Helton et al. 2024). However, our LAE comparison shows no strong correlation between Lyman- $\alpha$  visibility and overdensity in GOODS-N/S, indicating that the presence of LAEs is not defined by environment alone. This may partly reflect the range of Lyman- $\alpha$  EWs included in our sample, as studies focusing on the strongest emitters ( $EW > 100 \text{ \AA}$ ) have found a clearer association with overdense regions (e.g. Chen et al. 2025). Bright galaxies may contribute to the formation of larger ionized regions (e.g. Tang et al. 2024; Witstok et al. 2024), but Lyman- $\alpha$  visibility likely also depends on more local conditions within and around individual galaxies. Thus, bright-galaxy clustering traces the underlying structure, while LAE visibility reflects additional small-scale effects.

Possible galaxy mergers also appear to provide a hint that they may be an important factor affecting Lyman- $\alpha$  visibility. Several close galaxy pairs, including GN\_29192 and GN\_29193, GS\_6644 and GS\_6645, GS\_12667 and GS\_12669, GS\_23161 and GS\_23162, suggest the possibility of ongoing or recent interactions. While some of these pairs are detected as LAEs, others are not confirmed as such, though they could potentially be LAEs. The presence of LAEs in these pairs likely contributes to their detection, but even non-LAEs may still play a role. These non-LAE galaxies might ionize the region around them, creating an environment that allows Lyman- $\alpha$  photons from neighbouring galaxies to pass through the ionized medium, depending on the line of sight. This highlights the possibility that mergers could enhance Lyman- $\alpha$  emission through triggered star formation or AGN activity, affecting the surrounding ionization and contributing to the observed properties of LAEs in dynamically active environments.

The contribution of AGN to Lyman- $\alpha$  visibility is another aspect that requires further exploration. In the group GN\_z7\_2, which includes the AGN GN\_5688 (Fujimoto et al. 2022), we identify a potential AGN, GN\_14101, that could provide additional ionizing radiation, contributing to local reionization. The presence of potential AGNs in these regions raises important questions about their role in ionized bubble formation and their potential contribution to

facilitating Lyman- $\alpha$  escape at high redshift. It is also worth noting that GN\_26844, which is an LAE, has a companion LAE, GN\_4394, with a very large equivalent width of  $221 \text{ \AA}$ . The high EW and stellar mass ( $\log_{M_\star} \sim 9$ ) of GN\_4394 suggest that it could also potentially host an AGN, adding complexity to the dynamics of the GN\_z7\_2 group.

Finally, Lyman- $\alpha$  visibility may depend not only on the physical properties of galaxies and their environments but also on observational effects such as viewing angles and the geometry of ionized regions (e.g. Rosdahl et al. 2018; Katz et al. 2020; Garel et al. 2021). The lack of a clear distinction in overdensity measurements between LAEs and non-LAE [OIII] emitters suggests that the detectability of Lyman- $\alpha$  emission may be influenced by the orientation of ionized bubbles relative to the observer. If Lyman- $\alpha$  photons are more likely to escape along certain sightlines, this could explain why some galaxies in dense environments do not appear as LAEs despite having similar intrinsic properties.

Overall, our findings highlight the complexity of Lyman- $\alpha$  visibility at  $7 < z < 8$ . The combination of environmental and intrinsic factors, together with observational effects such as viewing angles, shapes the conditions under which Lyman- $\alpha$  photons can escape and be detected. While bright galaxies are often found in clustered regions that may contribute to large-scale reionization (e.g. Castellano et al. 2018; Endsley & Stark 2022; Stark et al. 2017; Leonova et al. 2022; Larson et al. 2022; Tang et al. 2024; Witstok et al. 2024), our results indicate that Lyman- $\alpha$  visibility is not solely determined by local overdensity. Instead, other factors, including mergers, AGN activity, or ionized bubble geometry — could influence Lyman- $\alpha$  visibility. In addition, ultra-faint galaxies, undetected by the FRESCO survey, may contribute to reionization by producing small ionized regions that allow Lyman- $\alpha$  photons to escape.

## 5 SUMMARY

In this study, we investigated the spatial distribution and intrinsic properties of LAEs and [OIII] emitters at redshifts  $7 < z < 8$  using FRESCO NIRCcam/grism data from the GOODS-N and GOODS-S fields. Our goal was to determine the relative contributions of environmental and intrinsic factors in regulating Lyman- $\alpha$  visibility and to assess the role of these galaxies in the epoch of reionization. Our main results are:

- Using Keck archival data we discover 8 new LAEs in the GOODS-N field, expanding the known sample of high-redshift LAEs.
- In 3.1, we investigate the environment of LAEs at  $7 < z < 8$  by categorizing galaxies into four groups in GOODS-N and three in GOODS-S, each centered around the brightest LAE. Our results show that GOODS-N contains significant clustering of galaxies in the GN\_z7\_0 group, and potential mergers, such as in GN\_z7\_5. The GN\_z7\_6 group is also notable for containing four LAEs. In GOODS-S, the environment is marked by fewer bright [OIII] emitters, with notable objects like the faint LAE JADES-13682 in GS\_z7\_2, and a potential merger in GS\_z7\_7. Additionally, the role of AGNs in Lyman- $\alpha$  visibility is hinted by the presence of AGN GN\_5688 and potential AGNs in the GN\_z7\_2 group, including GN\_14101 and GN\_4394.
- In 3.2 we analyze the overdensity properties of LAEs compared to [OIII] emitters without detected Lyman- $\alpha$  emission by calculating the overdensity parameter using the UV luminosity function. We explore whether LAEs' presence in overdense regions, where ion-

ized bubbles enhance photon transmission, primarily explains their Lyman- $\alpha$  visibility. We find that the mean overdensity parameters for both groups are similar, suggesting that while LAEs are located in overdense regions, overdensity alone does not determine Lyman- $\alpha$  emission, indicating that other factors are likely involved in shaping Lyman- $\alpha$  escape.

- In 3.3 we examine physical properties of LAEs and non-LAE [OIII] emitters, such as UV magnitudes,  $\beta$  slopes, stellar masses, and  $EW_{\text{[OIII]}}$ . This comparison allows us to assess whether factors such as dust attenuation, ionizing photon production, or galaxy assembly history influence the emergence of Lyman- $\alpha$  emission. The slightly higher mean  $EW_{\text{[OIII]}}$  and  $SFR_{10}/SFR_{50}$  for LAEs could suggest more intense star formation and stronger ionizing radiation compared to non-LAE [OIII] emitters. However, in general all intrinsic properties, including the  $\beta$  slope, UV magnitude, and stellar mass are similar between LAEs and non-LAEs. This suggests that while LAEs may exhibit higher active star formation and stronger ionization, these factors alone do not fully explain the presence of Lyman- $\alpha$  emission.
- Our analysis shows that LAEs in GOODS-N and GOODS-S are not preferentially located in overdense regions, suggesting that large-scale environment alone does not determine Lyman- $\alpha$  visibility. However, we note a few cases with nearby companions, which may indicate small-scale interactions (e.g. mergers) that facilitate Lyman- $\alpha$  escape through enhanced star formation or AGN-driven ionization.

Our understanding of Lyman- $\alpha$  visibility at  $7 < z < 8$  will improve with more complete galaxy samples that include fainter sources and a confirmed classification of [OIII] emitters as LAEs. Future spectroscopic surveys in the FRESCO field (such as GO-9214; PIs: Mason & Stark), with broader wavelength coverage, will be essential for making these determinations. Identifying which [OIII] emitters are LAEs, along with detecting fainter sources, will provide deeper insight into the factors governing Lyman- $\alpha$  transmission, such as local ionization conditions, viewing angles, large-scale environment, and the role of low-luminosity galaxies.

## ACKNOWLEDGEMENTS

The work presented in this paper is based on observations made with the NASA/ESA/CSA James Webb Space Telescope. The data were obtained from the Mikulski Archive for Space Telescopes at the Space Telescope Science Institute, which is operated by the Association of Universities for Research in Astronomy, Inc., under NASA contract NAS 5-03127 for JWST. These observations are associated with program #1895.

This research has made use of the Keck Observatory Archive (KOA), which is operated by the W. M. Keck Observatory and the NASA Exoplanet Science Institute (NExScI), under contract with the National Aeronautics and Space Administration.

EL is grateful for financial support from the Nedelandse Organisatie voor Wetenschappelijk Onderzoek (NWO) through the NWO/Groot grant "Gravitational waves: The new cosmic messengers". This work has received funding from the Swiss State Secretariat for Education, Research and Innovation (SERI) under contract number MB22.00072, as well as from the Swiss National Science Foundation (SNSF) through project grant 200020\_207349. The

Cosmic Dawn Center (DAWN) is funded by the Danish National Research Foundation under grant DNRF140.

Telescope facilities: JWST (NIRCam, NIRSpec), Keck (MOS-FIRE)

## DATA AVAILABILITY

The JWST raw data products used in this work are available via the Mikulski Archive for Space Telescopes (<https://mast.stsci.edu>). The [OIII] emitter catalogs from Meyer et al. (2024) are available at <https://github.com/rameyer/fresco/>. The Keck spectra can be retrieved via <https://grizli-cutout.herokuapp.com/>. Additional data presented in this work will be made available by the authors upon request.

## REFERENCES

- Asthana S., Haehnelt M. G., Kulkarni G., Aubert D., Bolton J. S., Keating L. C., 2024, *MNRAS*, **533**, 2843
- Atek H., et al., 2009, *A&A*, **518**, A65
- Barkana R., Loeb A., 2001, *Phys. Rep.*, **349**, 125
- Begley R., et al., 2024, *arXiv e-prints*, p. [arXiv:2410.10988](https://arxiv.org/abs/2410.10988)
- Bhagwat A., Napolitano L., Pentericci L., Ciardi B., Costa T., 2025, *MNRAS*, **542**, 128
- Bouwens R. J., et al., 2021, *arXiv e-prints*, p. [arXiv:2102.07775](https://arxiv.org/abs/2102.07775)
- Boyett K., et al., 2024, *MNRAS*, **535**, 1796
- Castellano M., et al., 2018, *ApJ*, **863**, L3
- Castelli F., Kurucz R. L., 2003, in Piskunov N., Weiss W. W., Gray D. F., eds, IAU Symposium Vol. 210, *Modelling of Stellar Atmospheres*. p. A20 ([arXiv:astro-ph/0405087](https://arxiv.org/abs/astro-ph/0405087)), doi:10.48550/arXiv.astro-ph/0405087
- Chen Z., Stark D. P., Mason C., Topping M. W., Whitler L., Tang M., Endsley R., Charlot S., 2024, *MNRAS*, **528**, 7052
- Chen Z., Stark D. P., Mason C. A., Tang M., Whitler L., Lu T.-Y., Topping M. W., 2025, *arXiv e-prints*, p. [arXiv:2505.24080](https://arxiv.org/abs/2505.24080)
- Covelo-Paz A., et al., 2024, *arXiv e-prints*, p. [arXiv:2409.17241](https://arxiv.org/abs/2409.17241)
- D'Eugenio F., et al., 2024, *arXiv e-prints*, p. [arXiv:2404.06531](https://arxiv.org/abs/2404.06531)
- Dayal P., Ferrara A., 2018, *Phys. Rep.*, **780**, 1
- Dayal P., Maselli A., Ferrara A., 2011, *MNRAS*, **410**, 830
- Dayal P., et al., 2024, *arXiv e-prints*, p. [arXiv:2401.11242](https://arxiv.org/abs/2401.11242)
- Dijkstra M., 2014, *Publ. Astron. Soc. Australia*, **31**, e040
- Eisenstein D. J., et al., 2023, *arXiv e-prints*, p. [arXiv:2306.02465](https://arxiv.org/abs/2306.02465)
- Ellis R. S., 2025, *arXiv e-prints*, p. [arXiv:2508.16948](https://arxiv.org/abs/2508.16948)
- Endsley R., Stark D. P., 2022, *MNRAS*, **511**, 6042
- Endsley R., Stark D. P., Chevallard J., Charlot S., 2021, *MNRAS*, **500**, 5229
- Endsley R., et al., 2024, *MNRAS*, **533**, 1111
- Finkelstein S. L., et al., 2019, *ApJ*, **879**, 36
- Fujimoto S., et al., 2022, *Nature*, **604**, 261
- Gaia Collaboration et al., 2023, *A&A*, **674**, A1
- Garel T., Blaizot J., Rosdahl J., Katz H., Kimm T., Michel-Dansac L., Ocvirk P., Verhamme A., 2021, *MNRAS*, **504**, 1902
- Giallongo E., et al., 2015, *A&A*, **578**, A83
- Hashemi S., Becker G. D., Zhu Y., Hong H., 2025, *arXiv e-prints*, p. [arXiv:2507.16231](https://arxiv.org/abs/2507.16231)
- Hayes M. J., Scarlata C., 2023, *ApJ*, **954**, L14
- Hayes M., et al., 2011, *ApJ*, **730**, 8
- Helton J. M., et al., 2024, *ApJ*, **974**, 41
- Herard-Demanche T., et al., 2025, *MNRAS*, **542**, 128
- Hoag A., et al., 2019, *ApJ*, **878**, 12
- Hutter A., Dayal P., Müller V., Trott C. M., 2017, *ApJ*, **836**, 176
- Johnson B. D., Leja J., Conroy C., Speagle J. S., 2021, *ApJS*, **254**, 22
- Jones G. C., et al., 2025, *MNRAS*, **536**, 2355
- Jung I., et al., 2020, *ApJ*, **904**, 144
- Jung I., et al., 2022, *arXiv e-prints*, p. [arXiv:2212.09850](https://arxiv.org/abs/2212.09850)
- Kageura Y., et al., 2025, *arXiv e-prints*, p. [arXiv:2501.05834](https://arxiv.org/abs/2501.05834)
- Kashino D., et al., 2025, *arXiv e-prints*, p. [arXiv:2506.03121](https://arxiv.org/abs/2506.03121)

- Katz H., et al., 2020, *MNRAS*, 498, 164
- Kolmogorov A. N., Smirnov N., 1933, *Giornale dell’Istituto Italiano degli Attuari / Ann. Math. Stat.*
- Larson R. L., et al., 2022, arXiv e-prints, p. arXiv:2203.08461
- Leonova E., et al., 2022, *MNRAS*, 515, 5790
- Lu T.-Y., et al., 2024, arXiv e-prints, p. arXiv:2411.04176
- Lu T.-Y., et al., 2025, *A&A*, 697, A69
- Martin C. L., et al., 2025, arXiv e-prints, p. arXiv:2510.13140
- Mason C. A., Treu T., Dijkstra M., Mesinger A., Trenti M., Pentericci L., de Barros S., Vanzella E., 2018a, *ApJ*, 856, 2
- Mason C. A., et al., 2018b, *ApJ*, 857, L11
- Matharu J., et al., 2024, *A&A*, 690, A64
- Matthee J., Sobral D., Darvish B., Santos S., Mobasher B., Paulino-Afonso A., Röttgering H., Alegre L., 2017, *MNRAS*, 472, 772
- Matthee J., Sobral D., Gronke M., Paulino-Afonso A., Stefanon M., Röttgering H., 2018, *A&A*, 619, A136
- Matthee J., et al., 2022, *MNRAS*, 512, 5960
- Matthee J., Mackenzie R., Simcoe R. A., Kashino D., Lilly S. J., Bordoloi R., Eilers A.-C., 2023, *ApJ*, 950, 67
- Matthee J., et al., 2024, *ApJ*, 963, 129
- McQuinn M., Lidz A., Zahn O., Dutta S., Hernquist L., Zaldarriaga M., 2007, *MNRAS*, 377, 1043
- Meyer R. A., Laporte N., Ellis R. S., Verhamme A., Garel T., 2021, *MNRAS*, 500, 558
- Meyer R. A., et al., 2024, *MNRAS*, 535, 1067
- Miralda-Escudé J., 1998, *ApJ*, 501, 15
- Naidu R. P., Tacchella S., Mason C. A., Bose S., Oesch P. A., Conroy C., 2020, *ApJ*, 892, 109
- Naidu R. P., et al., 2024, arXiv e-prints, p. arXiv:2410.01874
- Napolitano L., et al., 2024, *A&A*, 688, A106
- Napolitano L., et al., 2025, arXiv e-prints, p. arXiv:2508.14171
- Nelson E., et al., 2024, *ApJ*, 976, L27
- Neyer M., Smith A., Vogelsberger M., Ángela García L., Kannan R., Garaldi E., Keating L., 2025, arXiv e-prints, p. arXiv:2510.18946
- Oesch P. A., et al., 2023, *MNRAS*, 525, 2864
- Oke J. B., Gunn J. E., 1983, *ApJ*, 266, 713
- Ouchi M., Ono Y., Shibuya T., 2020, *ARA&A*, 58, 617
- Pentericci L., et al., 2011, *ApJ*, 743, 132
- Planck Collaboration et al., 2020, *A&A*, 641, A6
- Prieto-Lyon G., et al., 2025, arXiv e-prints, p. arXiv:2509.18302
- Roberts-Borsani G., et al., 2023, *ApJ*, 948, 54
- Robertson B. E., 2022, *ARA&A*, 60, 121
- Rosdahl J., et al., 2018, *MNRAS*, 479, 994
- Saxena A., et al., 2023, arXiv e-prints, p. arXiv:2302.12805
- Saxena A., et al., 2024, *A&A*, 684, A84
- Smith A., Kannan R., Garaldi E., Vogelsberger M., Pakmor R., Springel V., Hernquist L., 2021, arXiv e-prints, p. arXiv:2110.02966
- Song M., Finkelstein S. L., Livermore R. C., Capak P. L., Dickinson M., Fontana A., 2016, *ApJ*, 826, 113
- Stark D. P., Ellis R. S., Chiu K., Ouchi M., Bunker A., 2010, *MNRAS*, 408, 1628
- Stark D. P., et al., 2017, *MNRAS*, 464, 469
- Stark D. P., Topping M. W., Endsley R., Tang M., 2026, in *Encyclopedia of Astrophysics*. pp 453–499, doi:10.1016/B978-0-443-21439-4.00128-0
- Tang M., et al., 2023, *MNRAS*, 526, 1657
- Tang M., Stark D. P., Topping M. W., Mason C., Ellis R. S., 2024, arXiv e-prints, p. arXiv:2408.01507
- Tang M., et al., 2025, *ApJ*, 991, 217
- Tilvi V., et al., 2020, *ApJ*, 891, L10
- Torralba-Torregrosa A., et al., 2024, *A&A*, 689, A44
- Umeda H., Ouchi M., Nakajima K., Harikane Y., Ono Y., Xu Y., Isobe Y., Zhang Y., 2024, *ApJ*, 971, 124
- Valentino F., et al., 2022, *ApJ*, 929, L9
- Virtanen P., Gommers R., Oliphant T. E., et al., 2020, *Nature Methods*, 17, 261
- Whitler L., Stark D. P., Mason C. A., Tang M., Chen Z., Lu T.-Y., Prieto-Lyon G., Hutter A., 2025, arXiv e-prints, p. arXiv:2510.12019
- Witstok J., et al., 2024, *A&A*, 682, A40
- Witstok J., et al., 2025, *MNRAS*, 536, 27
- Witten C., et al., 2024, *Nature Astronomy*, 8, 384
- Witten C., et al., 2025, arXiv e-prints, p. arXiv:2507.06284
- Xiao M., et al., 2024, *Nature*, 635, 311
- Xiao M., et al., 2025, No [CII] or dust detection in two Little Red Dots at  $z_{\text{spec}} > 7$  (arXiv:2503.01945), <https://arxiv.org/abs/2503.01945>
- Yung L. Y. A., Somerville R. S., Finkelstein S. L., Hirschmann M., Davé R., Popping G., Gardner J. P., Venkatesan A., 2021, *MNRAS*, 508, 2706
- Zitrin A., et al., 2015, *ApJ*, 810, L12

## APPENDIX A: APPENDIX

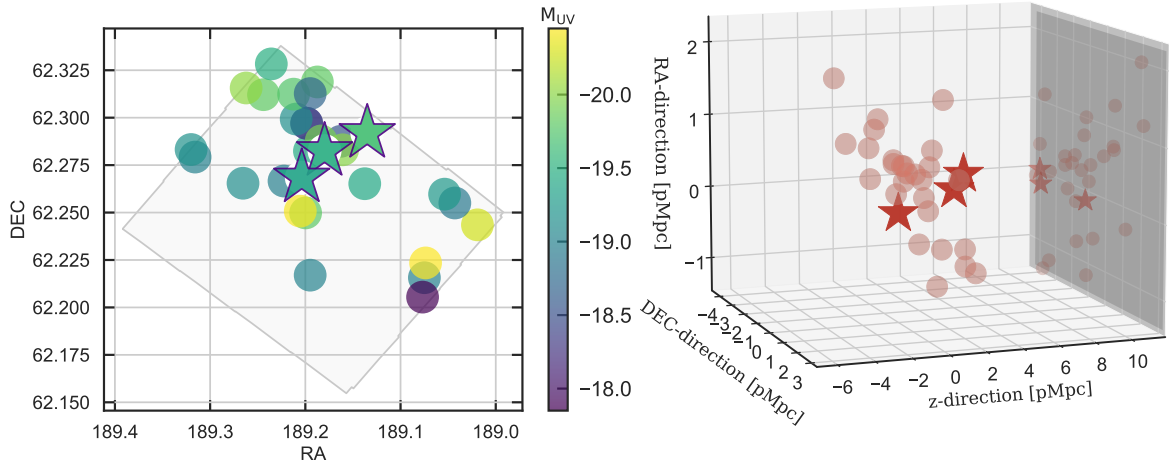
This paper has been typeset from a  $\text{\LaTeX}$  file prepared by the author.



ID	RA	DEC	$z_{\text{Ly}\alpha}$ <sup>c</sup>	$z_{[\text{OIII}]}$ <sup>d</sup>	$M_{\text{UV}}$	$\log M_{\star}$	$\text{EW}_{[\text{OIII}]}[\text{\AA}]$ <sup>e</sup>
<b>GN_z7_0 group</b>							
27795 <sup>a</sup>	189.13498	62.29190	7.038	7.017	-19.6 <sup>+0.1</sup> <sub>-0.1</sub>	7.59 <sup>+0.15</sup> <sub>-0.08</sub>	1263 <sup>+125</sup> <sub>-121</sub>
26051 <sup>b 1</sup>	189.17981	62.28239	7.087	7.084	-19.5 <sup>+0.1</sup> <sub>-0.1</sub>	7.60 <sup>+0.24</sup> <sub>-0.07</sub>	2371 <sup>+222</sup> <sub>-260</sub>
22679 <sup>b 1</sup>	189.20377	62.26843	7.09	7.090	-19.4 <sup>+0.1</sup> <sub>-0.1</sub>	7.51 <sup>+0.12</sup> <sub>-0.04</sub>	1839 <sup>+155</sup> <sub>-222</sub>
24082	189.07370	62.22345	-	7.035	-20.5 <sup>+0.0</sup> <sub>-0.1</sub>	8.18 <sup>+0.24</sup> <sub>-0.06</sub>	298 <sup>+45</sup> <sub>-34</sub>
17367	189.20531	62.25077	-	6.993	-20.4 <sup>+0.1</sup> <sub>-0.0</sub>	8.57 <sup>+0.10</sup> <sub>-0.13</sub>	820 <sup>+89</sup> <sub>-69</sub>
14967	189.01924	62.24353	-	7.038	-20.2 <sup>+0.0</sup> <sub>-0.1</sub>	9.25 <sup>+0.28</sup> <sub>-0.37</sub>	563 <sup>+40</sup> <sub>-59</sub>
30464	189.26217	62.31565	-	7.003	-20.0 <sup>+0.1</sup> <sub>-0.1</sub>	9.26 <sup>+0.37</sup> <sub>-0.99</sub>	373 <sup>+599</sup> <sub>-73</sub>
5412	189.16078	62.28308	-	7.045	-20.0 <sup>+0.1</sup> <sub>-0.0</sub>	8.28 <sup>+0.22</sup> <sub>-0.37</sub>	289 <sup>+54</sup> <sub>-48</sub>
27094	189.18337	62.28774	-	7.022	-19.9 <sup>+0.1</sup> <sub>-0.1</sub>	8.50 <sup>+0.39</sup> <sub>-0.48</sub>	398 <sup>+79</sup> <sub>-79</sub>
30164	189.24393	62.31213	-	7.072	-19.8 <sup>+0.1</sup> <sub>-0.1</sub>	7.98 <sup>+0.37</sup> <sub>-0.18</sub>	715 <sup>+134</sup> <sub>-130</sub>
30668	189.18736	62.31884	-	6.998	-19.9 <sup>+0.1</sup> <sub>-0.1</sub>	8.05 <sup>+0.46</sup> <sub>-0.25</sub>	396 <sup>+115</sup> <sub>-94</sub>
16993	189.19970	62.24981	-	6.992	-19.8 <sup>+0.1</sup> <sub>-0.0</sub>	8.14 <sup>+0.28</sup> <sub>-0.38</sub>	393 <sup>+64</sup> <sub>-57</sub>
30187	189.21231	62.31240	-	7.035	-19.8 <sup>+0.1</sup> <sub>-0.1</sub>	7.93 <sup>+0.38</sup> <sub>-0.19</sub>	440 <sup>+112</sup> <sub>-78</sub>
169	189.23573	62.32835	-	7.001	-19.5 <sup>+0.1</sup> <sub>-0.1</sub>	8.15 <sup>+0.41</sup> <sub>-0.61</sub>	492 <sup>+157</sup> <sub>-133</sub>
26059	189.19570	62.28243	-	7.091	-19.4 <sup>+0.1</sup> <sub>-0.1</sub>	8.71 <sup>+0.51</sup> <sub>-0.65</sub>	356 <sup>+116</sup> <sub>-57</sub>
21799	189.13759	62.26521	-	7.040	-19.4 <sup>+0.1</sup> <sub>-0.1</sub>	8.64 <sup>+0.38</sup> <sub>-0.47</sub>	363 <sup>+60</sup> <sub>-60</sub>
20218	189.05374	62.25970	-	7.084	-19.3 <sup>+0.1</sup> <sub>-0.1</sub>	7.57 <sup>+0.18</sup> <sub>-0.11</sub>	1626 <sup>+185</sup> <sub>-247</sub>
5365	189.31999	62.28323	-	7.074	-19.2 <sup>+0.1</sup> <sub>-0.1</sub>	7.87 <sup>+0.62</sup> <sub>-0.44</sub>	780 <sup>+360</sup> <sub>-206</sub>
28812	189.20960	62.29928	-	7.026	-18.8 <sup>+0.2</sup> <sub>-0.1</sub>	8.20 <sup>+0.29</sup> <sub>-0.35</sub>	373 <sup>+84</sup> <sub>-84</sub>
10162	189.26546	62.26544	-	6.983	-19.1 <sup>+0.1</sup> <sub>-0.1</sub>	8.44 <sup>+0.30</sup> <sub>-0.61</sub>	1702 <sup>+764</sup> <sub>-325</sub>
7409	189.19492	62.21700	-	7.019	-19.0 <sup>+0.0</sup> <sub>-0.1</sub>	7.70 <sup>+0.14</sup> <sub>-0.30</sub>	1259 <sup>+161</sup> <sub>-116</sub>
25360	189.31580	62.27925	-	6.943	-19.0 <sup>+0.3</sup> <sub>-0.2</sub>	8.54 <sup>+0.35</sup> <sub>-0.38</sub>	520 <sup>+87</sup> <sub>-87</sub>
7092	189.07495	62.21567	-	7.061	-19.0 <sup>+0.2</sup> <sub>-0.2</sub>	7.60 <sup>+0.24</sup> <sub>-0.09</sub>	989 <sup>+183</sup> <sub>-253</sub>
9825	189.22239	62.26662	-	6.948	-19.0 <sup>+0.1</sup> <sub>-0.1</sub>	7.57 <sup>+0.14</sup> <sub>-0.20</sub>	1086 <sup>+274</sup> <sub>-203</sub>
18770	189.04297	62.25504	-	7.096	-18.9 <sup>+0.3</sup> <sub>-0.2</sub>	8.35 <sup>+0.43</sup> <sub>-0.67</sub>	447 <sup>+236</sup> <sub>-113</sub>
30222	189.19487	62.31272	-	7.057	-18.7 <sup>+0.2</sup> <sub>-0.3</sub>	8.51 <sup>+0.35</sup> <sub>-0.32</sub>	571 <sup>+126</sup> <sub>-126</sub>
27069	189.16280	62.28755	-	7.013	-18.6 <sup>+0.3</sup> <sub>-0.2</sub>	8.91 <sup>+0.17</sup> <sub>-0.23</sub>	247 <sup>+53</sup> <sub>-53</sub>
28523	189.19861	62.29704	-	7.032	-18.4 <sup>+0.3</sup> <sub>-0.2</sub>	8.95 <sup>+0.18</sup> <sub>-0.19</sub>	358 <sup>+77</sup> <sub>-48</sub>
28524	189.19861	62.29704	-	7.042	-19.6 <sup>+0.2</sup> <sub>-0.1</sub>	9.27 <sup>+0.28</sup> <sub>-0.45</sub>	272 <sup>+42</sup> <sub>-42</sub>
28378	189.07686	62.20544	-	6.998	-17.7 <sup>+0.5</sup> <sub>-0.5</sub>	8.29 <sup>+0.46</sup> <sub>-0.72</sub>	984 <sup>+515</sup> <sub>-258</sub>

**Table A1.** Summary of the GN\_z7\_0 group.

Notes: <sup>a,b</sup> LAEs, <sup>c</sup> spectroscopic redshift from Lyman- $\alpha$  emission line, <sup>d</sup> systemic redshift, <sup>e</sup> [OIII] equivalent width (Naidu et al. in preparation)  
References: <sup>1</sup> [Tang et al. \(2024\)](#)



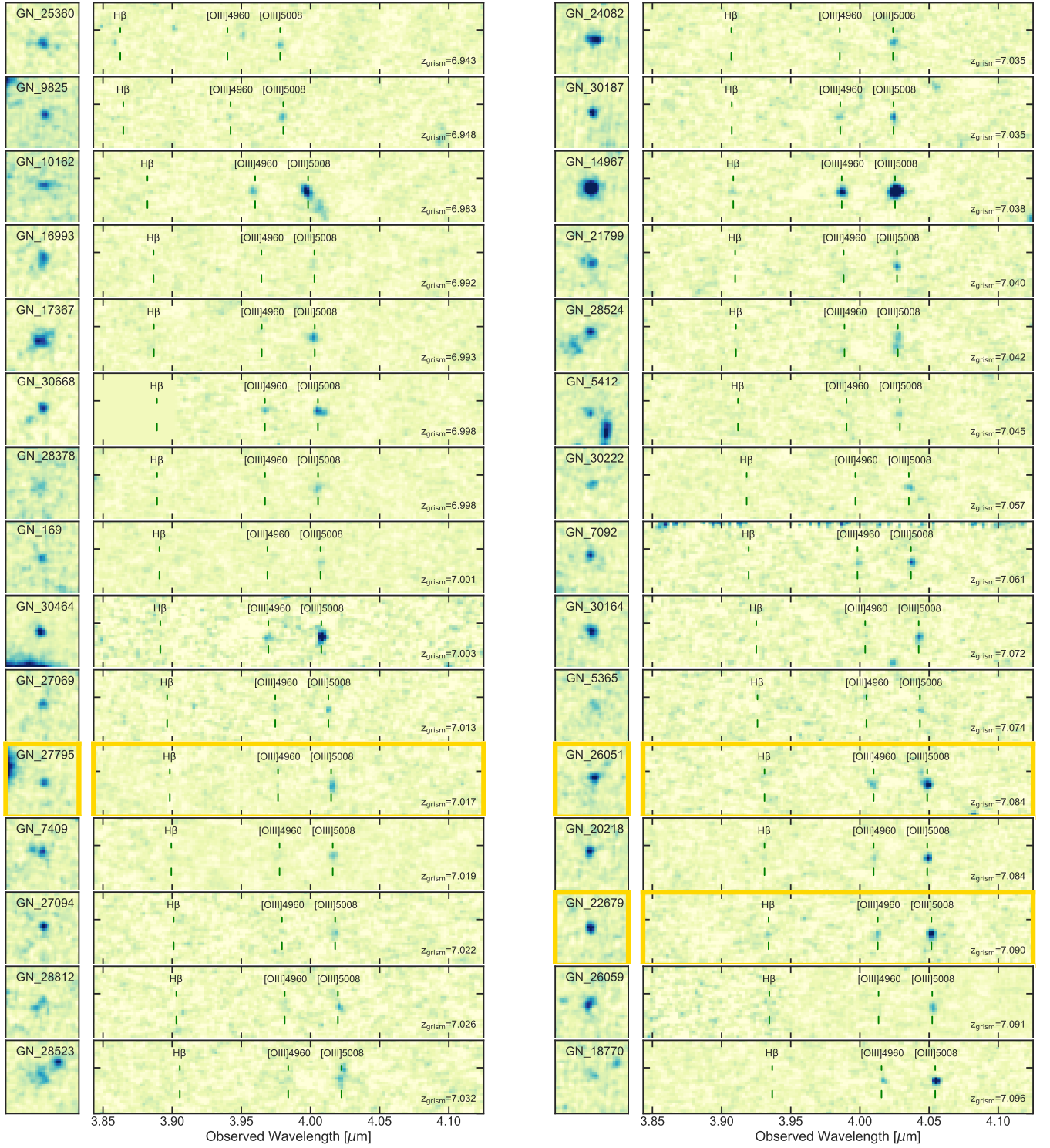


**Figure A1.** Top left panel: sky projection of galaxies in the GN\_z7\_0 group, where the LAE is marked as a star and its companion [OIII] emitters as circles. Top right panel: 3D spatial distribution, with the LAEs represented by stars and [OIII] emitters by circles. Axes are in proper Mpc, with redshift increasing along the x-axis. Bottom panel: 2D spectra of [OIII] emitters, with the yellow frame highlighting the Lyman- $\alpha$  emitters.

ID	RA	DEC	z <sub>Ly<math>\alpha</math></sub>	z <sub>[OIII]</sub>	M <sub>UV</sub>	log <sub>M<math>\star</math></sub>	EW <sub>[OIII]</sub> [Å]
<b>GN_z7_2 group</b>							
4394 <sup>a</sup>	189.08349	62.20258	7.197	7.186	-20.4 <sup>+0.1</sup> <sub>-0.1</sub>	9.15 <sup>+0.30</sup> <sub>-0.46</sub>	167 <sup>+73</sup> <sub>-25</sub>
8563 <sup>a</sup>	189.08405	62.22204	7.206	7.200	-20.2 <sup>+0.0</sup> <sub>-0.0</sub>	7.81 <sup>+0.12</sup> <sub>-0.07</sub>	816 <sup>+54</sup> <sub>-74</sub>
26844 <sup>a</sup>	189.22512	62.28629	7.21	7.205	-19.9 <sup>+0.1</sup> <sub>-0.1</sub>	7.84 <sup>+0.26</sup> <sub>-0.14</sub>	1306 <sup>+128</sup> <sub>-132</sub>
<b>GN_z7_2 group</b>							
5688 <sup>1</sup>	189.07065	62.20895	-	7.186	-22.8 <sup>+0.0</sup> <sub>-0.0</sub>	10.65 <sup>+0.11</sup> <sub>-0.10</sub>	7 <sup>+1</sup> <sub>-1</sub>
8877	189.13655	62.22330	-	7.139	-21.5 <sup>+0.0</sup> <sub>-0.0</sub>	8.50 <sup>+0.15</sup> <sub>-0.06</sub>	475 <sup>+31</sup> <sub>-26</sub>
5216	189.07460	62.20674	-	7.188	-21.2 <sup>+0.0</sup> <sub>-0.0</sub>	8.46 <sup>+0.66</sup> <sub>-0.18</sub>	500 <sup>+53</sup> <sub>-37</sub>
14101	189.24983	62.24122	-	7.145	-20.4 <sup>+0.0</sup> <sub>-0.0</sub>	8.62 <sup>+0.34</sup> <sub>-0.17</sub>	796 <sup>+53</sup> <sub>-49</sub>
19551	189.14817	62.23806	-	7.138	-20.4 <sup>+0.1</sup> <sub>-0.0</sub>	8.64 <sup>+0.42</sup> <sub>-0.13</sub>	437 <sup>+64</sup> <sub>-57</sub>
28784	189.24916	62.29901	-	7.134	-19.9 <sup>+0.1</sup> <sub>-0.1</sub>	8.86 <sup>+0.30</sup> <sub>-0.36</sub>	490 <sup>+79</sup> <sub>-79</sub>
256	189.15107	62.16643	-	7.166	-19.6 <sup>+0.2</sup> <sub>-0.1</sub>	8.07 <sup>+0.43</sup> <sub>-0.40</sub>	340 <sup>+120</sup> <sub>-81</sub>
20564	189.25929	62.23546	-	7.141	-19.4 <sup>+0.1</sup> <sub>-0.1</sub>	7.39 <sup>+0.07</sup> <sub>-0.04</sub>	327 <sup>+54</sup> <sub>-92</sub>
14140	189.25017	62.24139	-	7.150	-19.3 <sup>+0.1</sup> <sub>-0.0</sub>	7.95 <sup>+0.16</sup> <sub>-0.15</sub>	494 <sup>+68</sup> <sub>-95</sub>
12873	189.25888	62.23745	-	7.145	-19.2 <sup>+0.0</sup> <sub>-0.1</sub>	8.14 <sup>+0.08</sup> <sub>-0.65</sub>	806 <sup>+91</sup> <sub>-91</sub>
814	189.19798	62.17702	-	7.138	-19.0 <sup>+0.1</sup> <sub>-0.0</sub>	7.72 <sup>+0.05</sup> <sub>-0.06</sub>	1789 <sup>+104</sup> <sub>-116</sub>
11400	189.12769	62.23260	-	7.131	-18.9 <sup>+0.2</sup> <sub>-0.1</sub>	8.19 <sup>+0.34</sup> <sub>-0.26</sub>	965 <sup>+261</sup> <sub>-261</sub>
13324	189.10994	62.23872	-	7.132	-18.0 <sup>+0.2</sup> <sub>-0.2</sub>	7.64 <sup>+0.23</sup> <sub>-0.24</sub>	793 <sup>+141</sup> <sub>-141</sub>
20960	189.23104	62.26238	-	7.169	-17.3 <sup>+0.6</sup> <sub>-0.5</sub>	7.90 <sup>+0.55</sup> <sub>-0.52</sub>	1028 <sup>+509</sup> <sub>-509</sub>

**Table A2.** Summary of the GN\_z7\_2 group.Notes: <sup>a</sup> LAEsReferences: <sup>1</sup> [Fujimoto et al. \(2022\)](#)

ID	RA	DEC	z <sub>Ly<math>\alpha</math></sub>	z <sub>[OIII]</sub>	M <sub>UV</sub>	log <sub>M<math>\star</math></sub>	EW <sub>[OIII]</sub> [Å]
<b>GN_z7_5 group</b>							
29193 <sup>a</sup>	189.15798	62.30240	7.507	7.502	-21.1 <sup>+0.0</sup> <sub>-0.0</sub>	8.25 <sup>+0.19</sup> <sub>-0.05</sub>	799 <sup>+54</sup> <sub>-31</sub>
29192 <sup>a 1</sup>	189.15779	62.30234	7.507	7.498	-20.8 <sup>+0.0</sup> <sub>-0.0</sub>	8.22 <sup>+0.26</sup> <sub>-0.11</sub>	939 <sup>+126</sup> <sub>-96</sub>
<b>GN_z7_5 group</b>							
26237	189.26166	62.28327	-	7.427	-19.6 <sup>+0.1</sup> <sub>-0.1</sub>	7.73 <sup>+0.23</sup> <sub>-0.12</sub>	1455 <sup>+265</sup> <sub>-217</sub>
6294	189.26206	62.21209	-	7.423	-19.5 <sup>+0.1</sup> <sub>-0.1</sub>	8.21 <sup>+0.09</sup> <sub>-0.09</sub>	781 <sup>+89</sup> <sub>-78</sub>
29409	189.08771	62.20013	-	7.544	-18.7 <sup>+0.3</sup> <sub>-0.3</sub>	8.43 <sup>+0.39</sup> <sub>-0.86</sub>	516 <sup>+244</sup> <sub>-151</sub>
22186	189.22427	62.26668	-	7.522	-18.7 <sup>+0.2</sup> <sub>-0.2</sub>	8.56 <sup>+0.35</sup> <sub>-0.50</sub>	413 <sup>+126</sup> <sub>-126</sub>
9329	189.26255	62.26825	-	7.552	-18.7 <sup>+0.2</sup> <sub>-0.2</sub>	8.13 <sup>+0.39</sup> <sub>-0.49</sub>	490 <sup>+168</sup> <sub>-134</sub>

**Table A3.** Summary of the GN\_z7\_5 group.Notes: <sup>a</sup> LAEsReferences: <sup>1</sup> [Jung et al. \(2020\)](#)

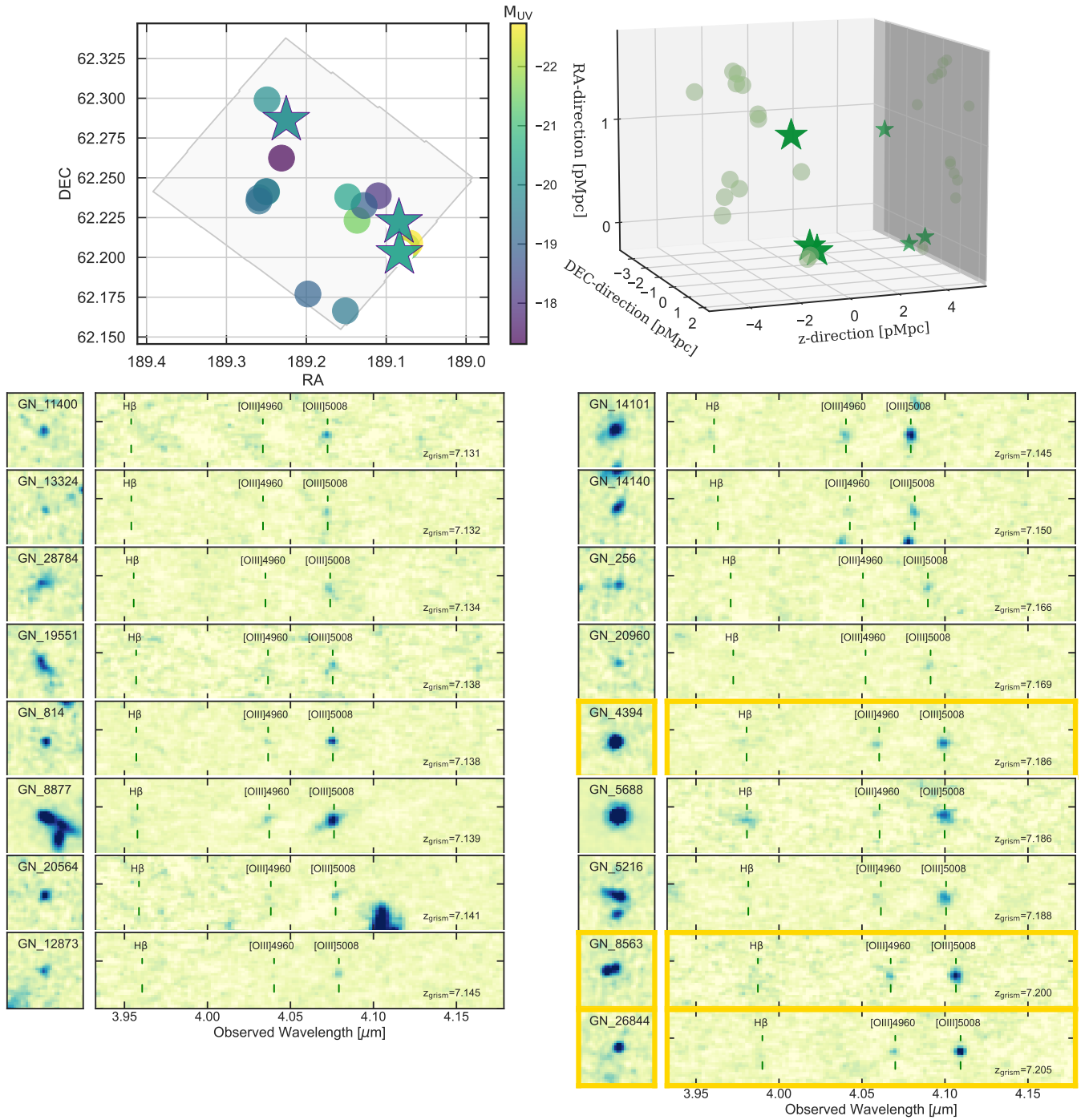


**Figure A2.** Top left panel: sky projection of galaxies in the GN\_z7\_2 group, where the LAE is marked as a star and its companion [OIII] emitters as circles. Top right panel: 3D spatial distribution, with the LAEs represented by stars and [OIII] emitters by circles. Axes are in proper Mpc, with redshift increasing along the x-axis. Bottom panel: 2D spectra of [OIII] emitters, with the yellow frame highlighting the Lyman- $\alpha$  emitters.



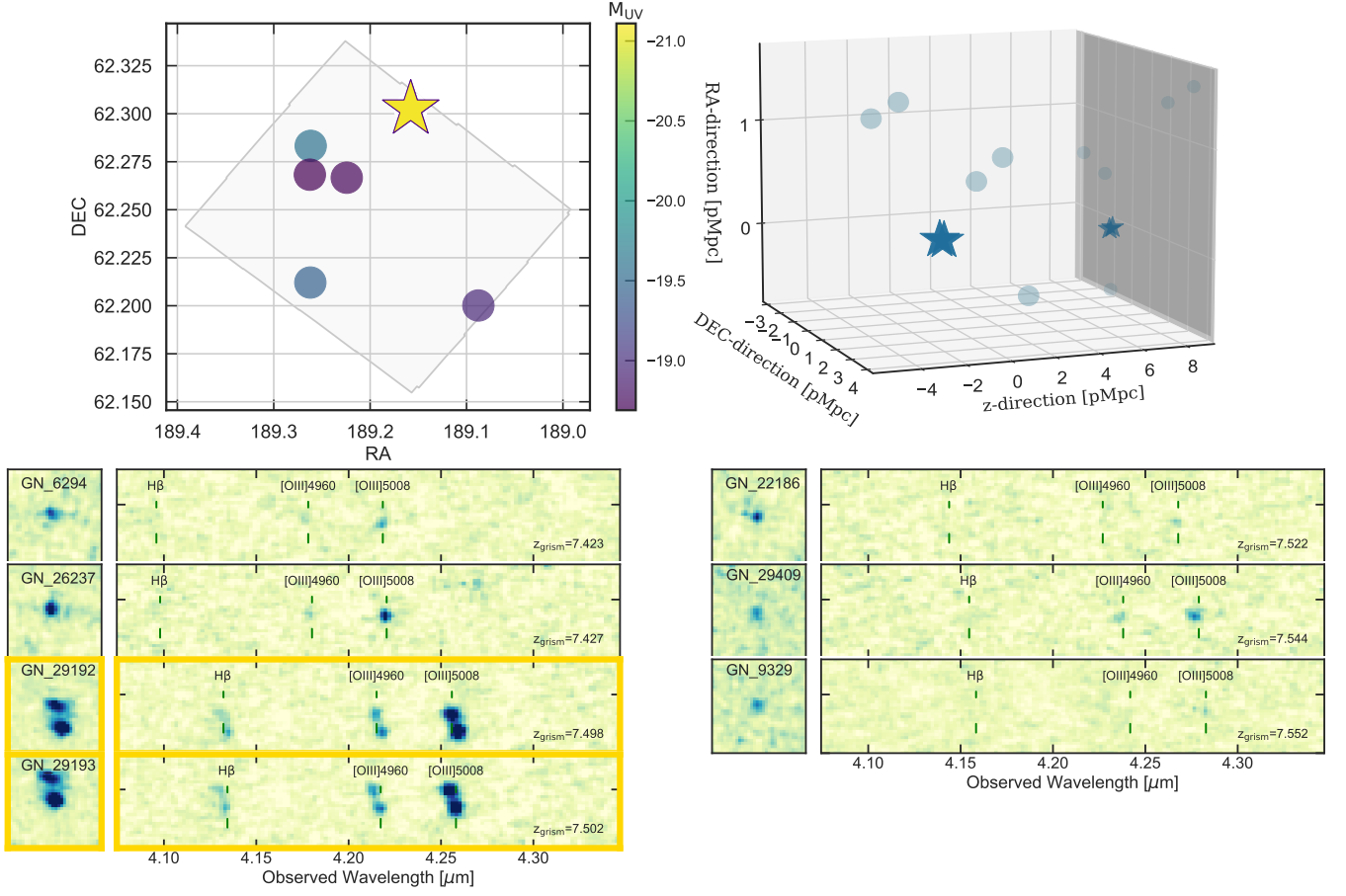


**Figure A3.** Top left panel: sky projection of galaxies in the GN\_z7\_5 group, where the LAE is marked as a star and its companion [OIII] emitters as circles. Top right panel: 3D spatial distribution, with the LAEs represented by stars and [OIII] emitters by circles. Axes are in proper Mpc, with redshift increasing along the x-axis. Bottom panel: 2D spectra of [OIII] emitters, with the yellow frame highlighting the Lyman- $\alpha$  emitters.

ID	RA	DEC	$z_{\text{Ly}\alpha}$	$z_{\text{[OIII]}}$	$M_{\text{UV}}$	$\log M_{\star}$	$\text{EW}_{\text{[OIII]}} [\text{\AA}]$
<b>GN_z7_6 group</b>							
19441 <sup>a1</sup>	189.33307	62.25722	7.6	7.595	-21.2 <sup>+0.0</sup> <sub>-0.0</sub>	8.33 <sup>+0.26</sup> <sub>-0.08</sub>	1930 <sup>+151</sup> <sub>-168</sub>
14535 <sup>a</sup>	189.20307	62.24249	7.657	7.648	-20.4 <sup>+0.1</sup> <sub>-0.1</sub>	8.61 <sup>+0.37</sup> <sub>-0.40</sub>	856 <sup>+159</sup> <sub>-75</sub>
25604 <sup>a</sup>	189.30014	62.28034	7.7	7.694	-19.9 <sup>+0.1</sup> <sub>-0.1</sub>	8.74 <sup>+0.40</sup> <sub>-0.26</sub>	439 <sup>+75</sup> <sub>-75</sub>
9680 <sup>a</sup>	189.28867	62.22651	7.635	7.629	-19.9 <sup>+0.1</sup> <sub>-0.0</sub>	8.15 <sup>+0.07</sup> <sub>-0.19</sub>	1028 <sup>+130</sup> <sub>-161</sub>
26281	189.20129	62.21439	-	7.647	-21.1 <sup>+0.1</sup> <sub>-0.1</sub>	9.01 <sup>+0.19</sup> <sub>-0.24</sub>	141 <sup>+17</sup> <sub>-23</sub>
27240	189.27002	62.28855	-	7.629	-20.7 <sup>+0.1</sup> <sub>-0.0</sub>	8.82 <sup>+0.14</sup> <sub>-0.16</sub>	1214 <sup>+111</sup> <sub>-135</sub>
30094	189.22439	62.31137	-	7.620	-20.3 <sup>+0.1</sup> <sub>-0.1</sub>	8.10 <sup>+0.56</sup> <sub>-0.08</sub>	819 <sup>+92</sup> <sub>-65</sub>
30469	189.22201	62.31576	-	7.600	-20.1 <sup>+0.1</sup> <sub>-0.1</sub>	7.87 <sup>+0.26</sup> <sub>-0.21</sub>	539 <sup>+87</sup> <sub>-81</sub>
16884	189.03149	62.24946	-	7.603	-19.7 <sup>+0.2</sup> <sub>-0.1</sub>	8.36 <sup>+0.55</sup> <sub>-0.43</sub>	447 <sup>+103</sup> <sub>-103</sub>
21941	189.06594	62.26573	-	7.607	-19.5 <sup>+0.1</sup> <sub>-0.1</sub>	8.16 <sup>+0.14</sup> <sub>-0.15</sub>	412 <sup>+115</sup> <sub>-115</sub>
16560	189.35297	62.24850	-	7.586	-19.4 <sup>+0.1</sup> <sub>-0.2</sub>	8.77 <sup>+0.34</sup> <sub>-0.36</sub>	341 <sup>+86</sup> <sub>-86</sub>
11294	189.33119	62.26185	-	7.595	-19.4 <sup>+0.1</sup> <sub>-0.1</sub>	8.31 <sup>+0.61</sup> <sub>-0.42</sub>	474 <sup>+115</sup> <sub>-121</sub>
14534	189.20319	62.24245	-	7.633	-19.2 <sup>+0.1</sup> <sub>-0.1</sub>	8.72 <sup>+0.28</sup> <sub>-0.28</sub>	655 <sup>+152</sup> <sub>-152</sub>
18605	189.04517	62.25453	-	7.651	-19.2 <sup>+0.2</sup> <sub>-0.2</sub>	8.05 <sup>+0.52</sup> <sub>-0.24</sub>	580 <sup>+198</sup> <sub>-163</sub>
28698	189.26083	62.29841	-	7.704	-18.6 <sup>+0.2</sup> <sub>-0.2</sub>	7.90 <sup>+0.47</sup> <sub>-0.30</sub>	747 <sup>+256</sup> <sub>-256</sub>
8328	189.17372	62.27178	-	7.613	-17.7 <sup>+0.5</sup> <sub>-0.5</sub>	7.84 <sup>+0.44</sup> <sub>-0.44</sub>	761 <sup>+266</sup> <sub>-242</sub>

**Table A4.** Summary of the GN\_z7\_6 group.Notes: <sup>a</sup> LAEsReferences: <sup>1</sup> Jung et al. (2020)

ID	RA	DEC	$z_{\text{Ly}\alpha}$	$z_{\text{[OIII]}}$	$M_{\text{UV}}$	$\log M_{\star}$	$\text{EW}_{\text{[OIII]}} [\text{\AA}]$
<b>GS_z7_2 group</b>							
1744 <sup>a</sup>	53.16958	-27.73806	7.242	7.242	-20.3 <sup>+0.0</sup> <sub>-0.0</sub>	8.21 <sup>+0.08</sup> <sub>-0.13</sub>	305 <sup>+75</sup> <sub>-49</sub>
JADES-13682 <sup>a12</sup>	53.16746	-27.7720	7.275 <sup>2</sup>	-	-16.7	-	-
23162	53.19540	-27.83548	-	7.276	-20.4 <sup>+0.1</sup> <sub>-0.1</sub>	8.69 <sup>+0.46</sup> <sub>-0.16</sub>	427 <sup>+39</sup> <sub>-57</sub>
12667	53.16481	-27.78826	-	7.231	-20.3 <sup>+0.0</sup> <sub>-0.0</sub>	8.12 <sup>+0.28</sup> <sub>-0.14</sub>	794 <sup>+80</sup> <sub>-74</sub>
12061	53.16171	-27.78539	-	7.236	-20.3 <sup>+0.1</sup> <sub>-0.0</sub>	9.36 <sup>+0.05</sup> <sub>-0.09</sub>	150 <sup>+29</sup> <sub>-29</sub>
23161	53.19541	-27.83543	-	7.277	-20.2 <sup>+0.1</sup> <sub>-0.0</sub>	7.90 <sup>+0.23</sup> <sub>-0.26</sub>	885 <sup>+129</sup> <sub>-116</sub>
14008	53.18373	-27.79390	-	7.261	-19.8 <sup>+0.1</sup> <sub>-0.1</sub>	8.36 <sup>+0.26</sup> <sub>-0.17</sub>	339 <sup>+46</sup> <sub>-46</sub>
12669	53.16469	-27.78823	-	7.249	-19.8 <sup>+0.0</sup> <sub>-0.0</sub>	8.29 <sup>+0.19</sup> <sub>-0.19</sub>	997 <sup>+95</sup> <sub>-95</sub>
13902	53.11354	-27.79349	-	7.168	-19.7 <sup>+0.0</sup> <sub>-0.0</sub>	7.80 <sup>+0.13</sup> <sub>-0.05</sub>	2332 <sup>+138</sup> <sub>-177</sub>
27493	53.07543	-27.85520	-	7.215	-19.6 <sup>+0.1</sup> <sub>-0.1</sub>	8.42 <sup>+0.04</sup> <sub>-0.03</sub>	1173 <sup>+139</sup> <sub>-139</sub>
5947	53.15086	-27.75734	-	7.255	-19.4 <sup>+0.1</sup> <sub>-0.1</sub>	8.65 <sup>+0.12</sup> <sub>-0.34</sub>	192 <sup>+37</sup> <sub>-37</sub>
9779	53.17975	-27.77465	-	7.275	-19.3 <sup>+0.0</sup> <sub>-0.0</sub>	8.29 <sup>+0.15</sup> <sub>-0.20</sub>	916 <sup>+66</sup> <sub>-66</sub>
4357	53.10019	-27.75030	-	7.221	-19.0 <sup>+0.2</sup> <sub>-0.2</sub>	8.74 <sup>+0.38</sup> <sub>-0.83</sub>	321 <sup>+257</sup> <sub>-65</sub>

**Table A5.** Summary of the GS\_z7\_2 group.Notes: <sup>a</sup> LAEs. JADES-13682 was not detected in FRESCO due to the sensitivity of the program.References: <sup>1</sup> Saxena et al. (2023), <sup>2</sup> Tang et al. (2024)

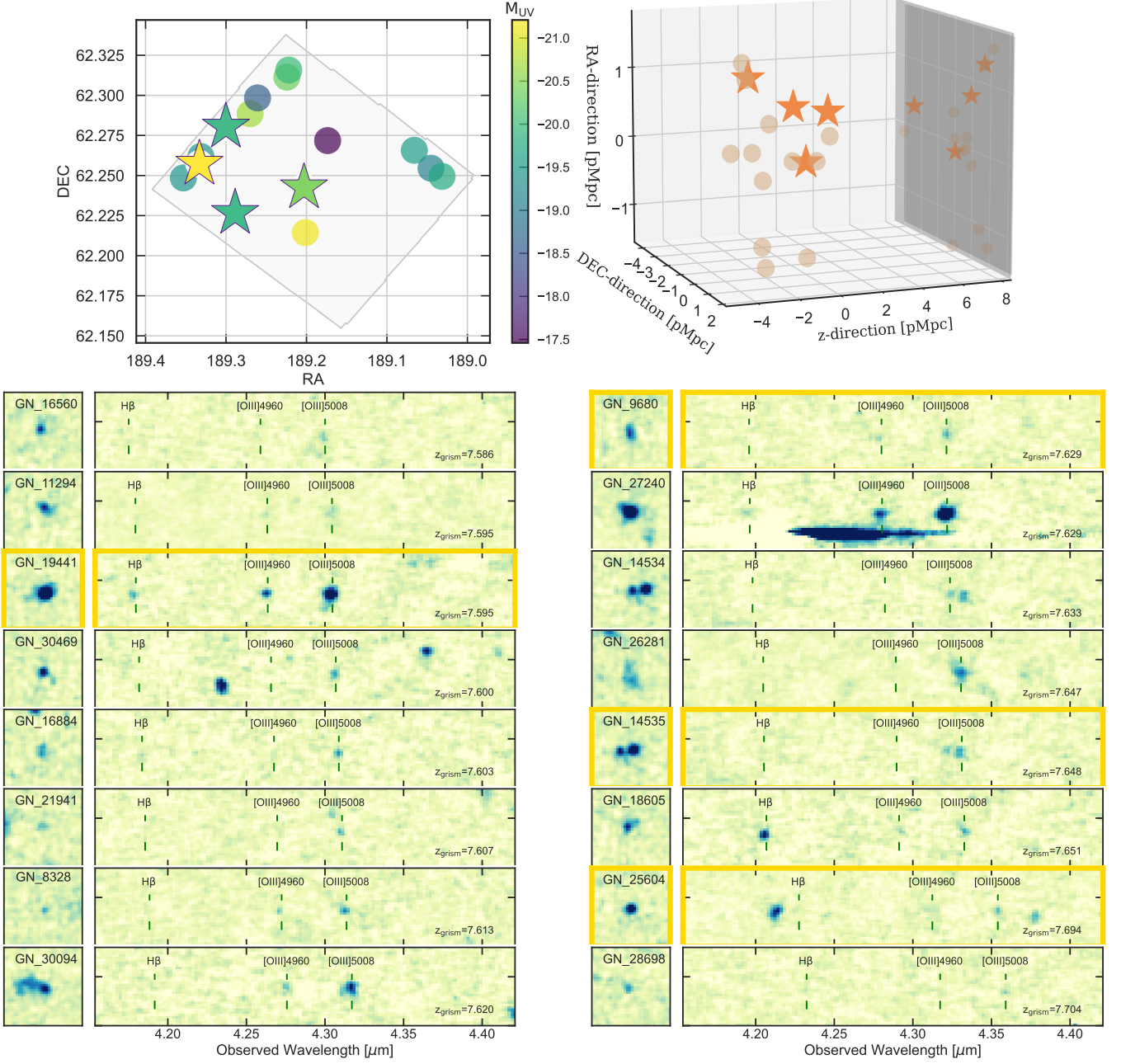


**Figure A4.** Top left panel: sky projection of galaxies in the GN<sub>z7\_6</sub> group, where the LAE is marked as a star and its companion [OIII] emitters as circles. Top right panel: 3D spatial distribution, with the LAE represented by stars and [OIII] emitters by circles. Axes are in proper Mpc, with redshift increasing along the x-axis. Bottom panel: 2D spectra of [OIII] emitters, with the yellow frame highlighting the Lyman- $\alpha$  emitters.

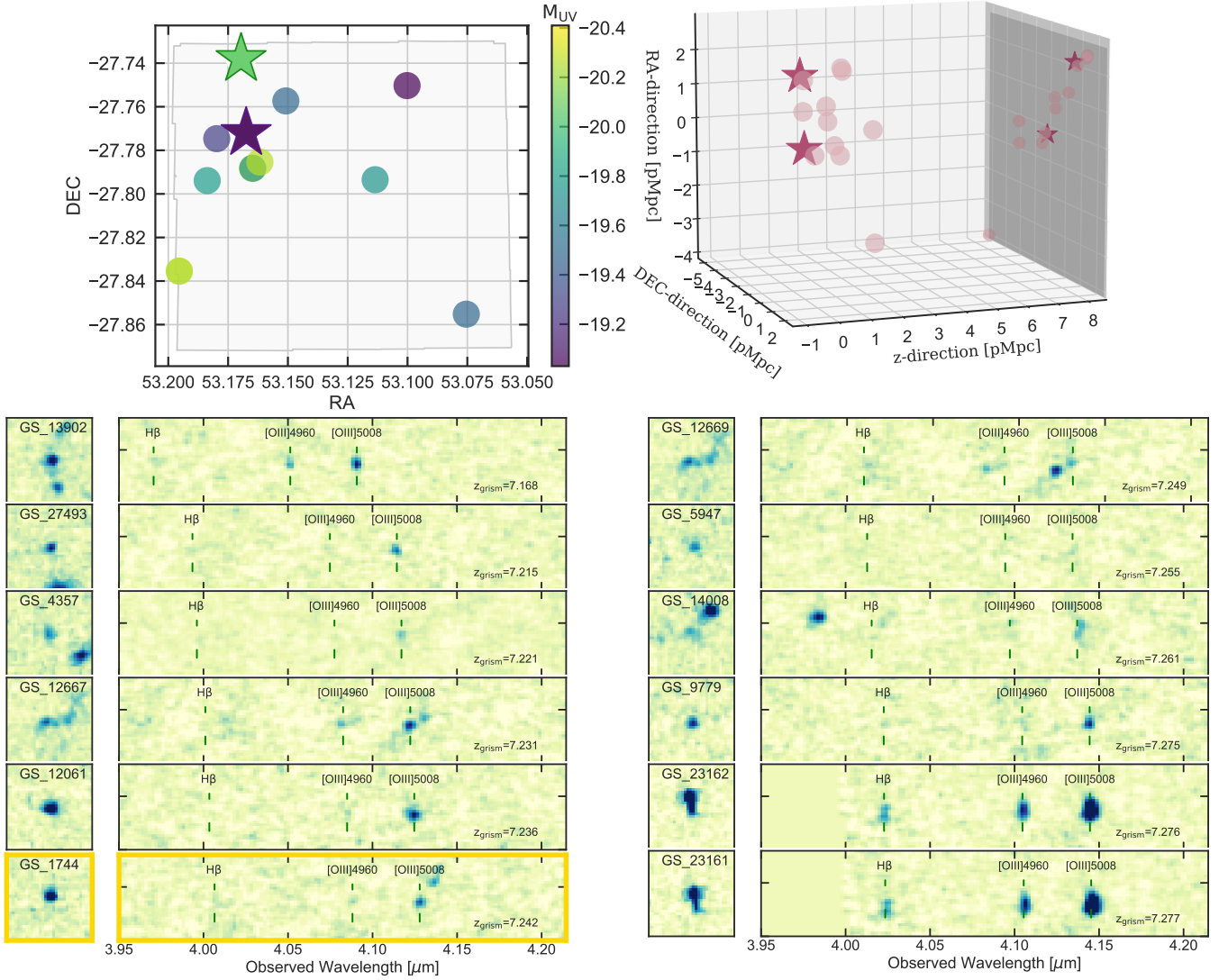


**Figure A5.** Top left panel: sky projection of galaxies in the GS\_z7\_2 group, where the LAE is marked as a star and its companion [OIII] emitters as circles. Top right panel: 3D spatial distribution, with the LAEs represented by stars and [OIII] emitters by circles. Axes are in proper Mpc, with redshift increasing along the x-axis. Bottom panel: 2D spectra of [OIII] emitters, with the yellow frame highlighting the Lyman- $\alpha$  emitters.

ID	RA	DEC	$z_{\text{Ly}\alpha}$	$z_{\text{[OIII]}}$	$M_{\text{UV}}$	$\log M_{\star}$	$\text{EW}_{\text{[OIII]}} [\text{\AA}]$
<b>GS_z7_7 group</b>							
6644 <sup>a12</sup>	53.13346	-27.76038	7.660	7.661	-20.8 <sup>+0.1</sup> <sub>-0.1</sub>	9.17 <sup>+0.48</sup> <sub>-0.34</sub>	262 <sup>+175</sup> <sub>-51</sub>
27780	53.12001	-27.85644	-	7.652	-20.4 <sup>+0.0</sup> <sub>-0.1</sub>	8.12 <sup>+0.40</sup> <sub>-0.37</sub>	723 <sup>+71</sup> <sub>-96</sub>
23584	53.15709	-27.83707	-	7.671	-20.3 <sup>+0.1</sup> <sub>-0.1</sub>	7.52 <sup>+0.28</sup> <sub>-0.06</sub>	1247 <sup>+148</sup> <sub>-116</sub>
17172	53.05892	-27.80809	-	7.681	-20.2 <sup>+0.1</sup> <sub>-0.1</sub>	9.43 <sup>+0.26</sup> <sub>-0.30</sub>	308 <sup>+64</sup> <sub>-31</sub>
20315	53.08631	-27.82396	-	7.6	-20.1 <sup>+0.0</sup> <sub>-0.1</sub>	7.66 <sup>+0.07</sup> <sub>-0.05</sub>	1367 <sup>+128</sup> <sub>-94</sub>
27775	53.12021	-27.85633	-	7.649	-19.9 <sup>+0.1</sup> <sub>-0.1</sub>	8.41 <sup>+0.20</sup> <sub>-0.43</sub>	885 <sup>+248</sup> <sub>-138</sub>
6645	53.13349	-27.76046	-	7.661	-19.5 <sup>+0.0</sup> <sub>-0.0</sub>	8.86 <sup>+0.09</sup> <sub>-0.13</sub>	383 <sup>+26</sup> <sub>-26</sub>

**Table A6.** Table of the GS\_z7\_7 group.

Notes: <sup>a</sup> LAE

References: <sup>1</sup> Song et al. (2016), <sup>2</sup> Tang et al. (2024)



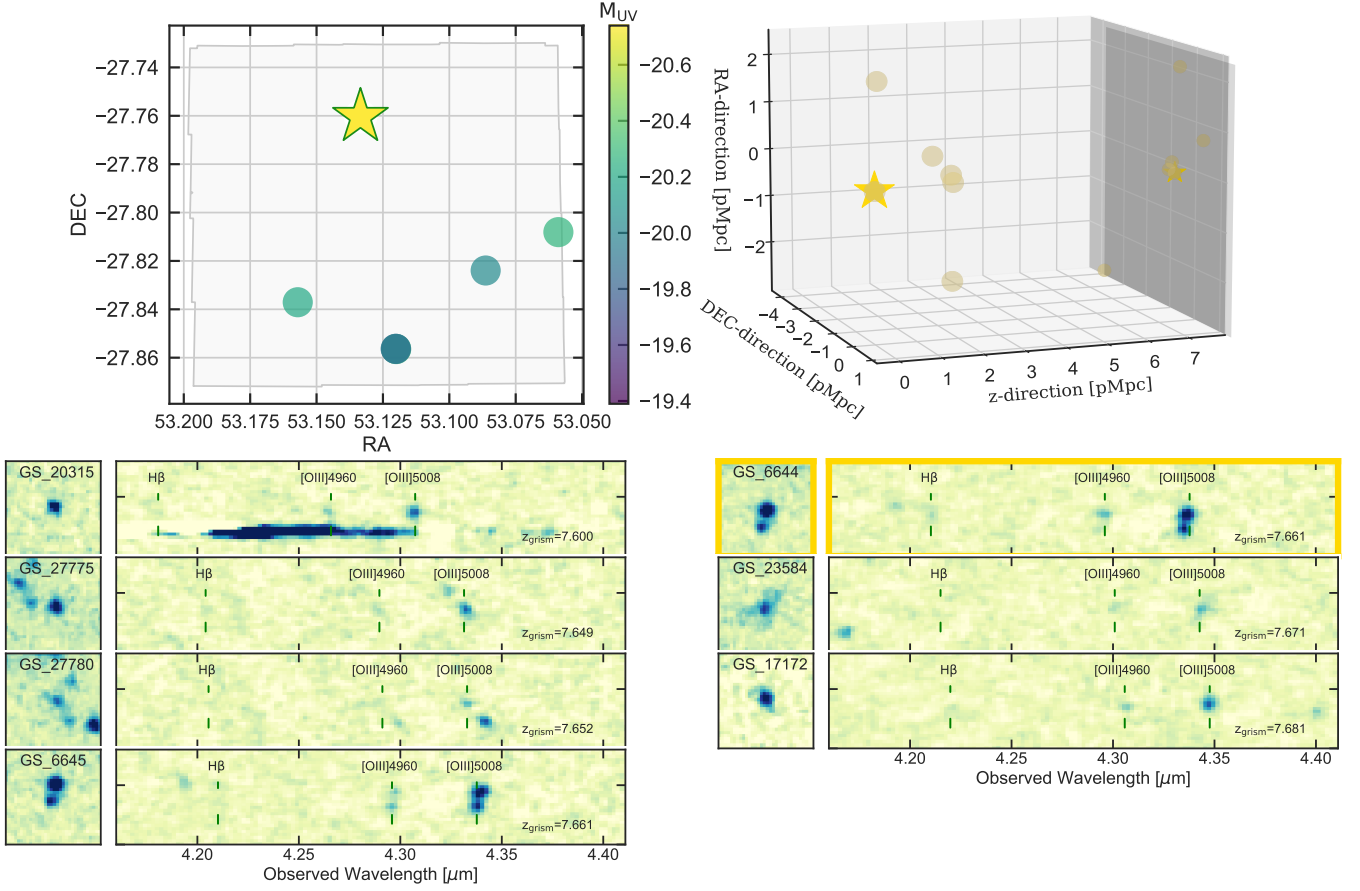


**Figure A6.** Top left panel: sky projection of galaxies in the GS\_z7\_7 group, where the LAE is marked as a star and its companion [OIII] emitters as circles. Top right panel: 3D spatial distribution, with the LAE represented by a star and [OIII] emitters by circles. Axes are in proper Mpc, with redshift increasing along the x-axis. Bottom panel: 2D spectra of [OIII] emitters, with the yellow frame highlighting the Lyman- $\alpha$  emitters.

ID	RA	DEC	$z_{\text{Ly}\alpha}$	$z_{[\text{OIII}]}$	$M_{\text{UV}}$	$\log M_{\star}$	$\text{EW}_{[\text{OIII}]} [\text{\AA}]$
<b>GS_z8 group</b>							
28631 <sup>a1</sup>	53.08738	-27.86031	7.962	7.958	-20.4 <sup>+0.0</sup> <sub>-0.0</sub>	8.59 <sup>+0.17</sup> <sub>-0.06</sub>	605 <sup>+48</sup> <sub>-52</sub>
284	53.06882	-27.73139	-	7.967	-21.3 <sup>+0.0</sup> <sub>-0.1</sub>	7.54 <sup>+0.20</sup> <sub>-0.06</sub>	742 <sup>+110</sup> <sub>-133</sub>
29419	53.06028	-27.86353	-	7.885	-19.7 <sup>+0.1</sup> <sub>-0.1</sub>	8.34 <sup>+0.37</sup> <sub>-0.09</sub>	789 <sup>+76</sup> <sub>-63</sub>
28440	53.08649	-27.85919	-	7.953	-19.7 <sup>+0.1</sup> <sub>-0.1</sub>	8.40 <sup>+0.14</sup> <sub>-0.18</sub>	416 <sup>+75</sup> <sub>-70</sub>
4864	53.19211	-27.75252	-	7.991	-18.9 <sup>+0.0</sup> <sub>-0.6</sub>	8.49 <sup>+0.39</sup> <sub>-0.64</sub>	705 <sup>+475</sup> <sub>-205</sub>
8102	53.15683	-27.76717	-	7.982	-18.8 <sup>+0.1</sup> <sub>-0.1</sub>	7.52 <sup>+0.36</sup> <sub>-0.26</sub>	823 <sup>+204</sup> <sub>-154</sub>
5402	53.10354	-27.75481	-	7.908	-17.9 <sup>+0.1</sup> <sub>-0.1</sub>	9.40 <sup>+0.18</sup> <sub>-0.21</sub>	415 <sup>+61</sup> <sub>-43</sub>

**Table A7.** Table of the GN\_z8 group.

Notes: <sup>a</sup> LAE

References: <sup>1</sup> [Roberts-Borsani et al. \(2023\)](#)

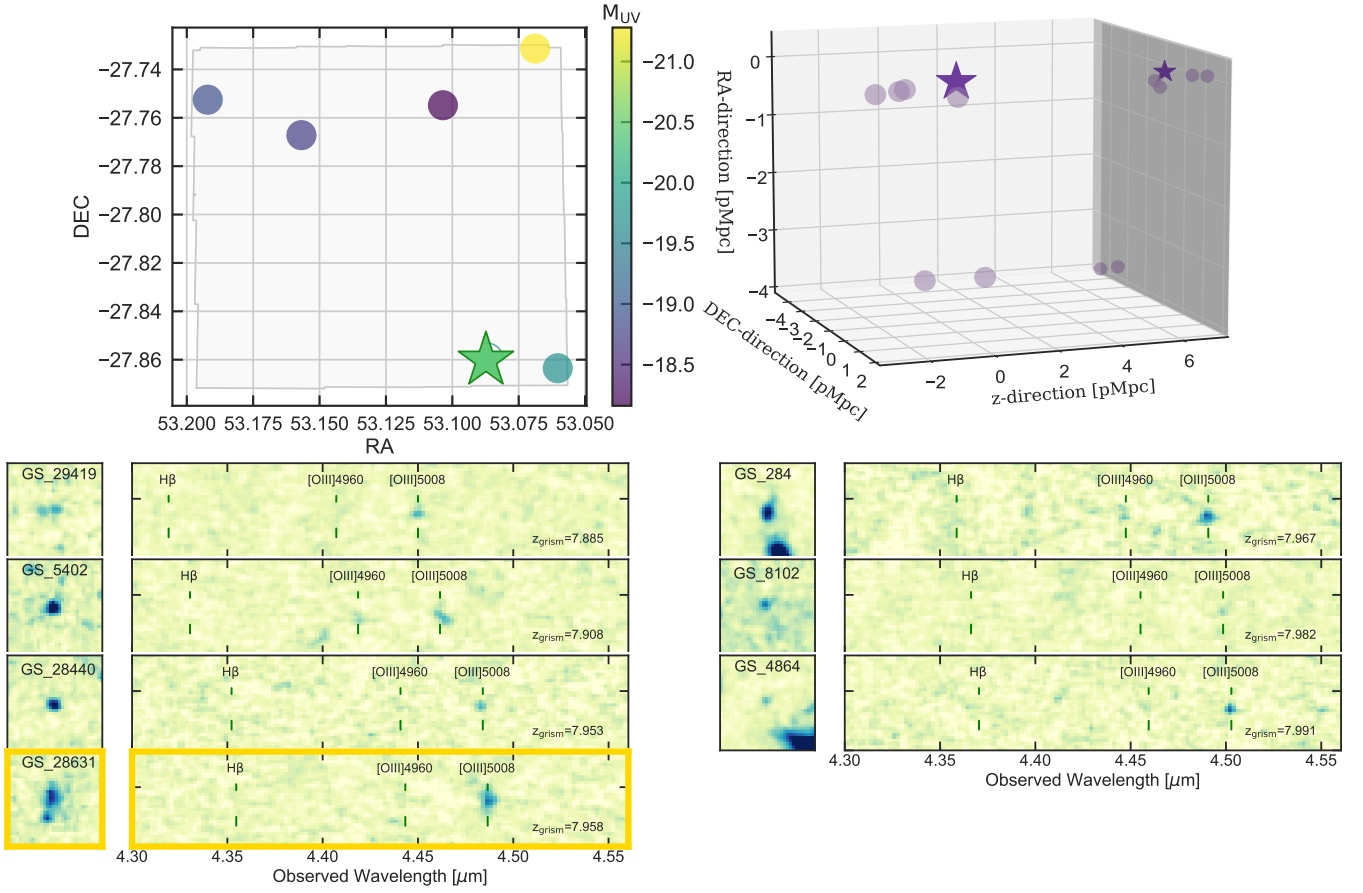


**Figure A7.** Top left panel: sky projection of galaxies in the GS\_z7\_8 group, where the LAE is marked as a star and its companion [OIII] emitters as circles. Top right panel: 3D spatial distribution, with the LAE represented by a star and [OIII] emitters by circles. Axes are in proper Mpc, with redshift increasing along the x-axis. Bottom panel: 2D spectra of [OIII] emitters, with the yellow frame highlighting the Lyman- $\alpha$  emitters.